



AFRL-RZ-WP-TR-2010-2073

**POWER AND THERMAL TECHNOLOGIES FOR AIR AND
SPACE – SCIENTIFIC RESEARCH PROGRAM**

Delivery Order 0015: High Performance Permanent Magnets

Christina Chen

University of Dayton Research Institute

MARCH 2010

Final Report

Approved for public release; distribution unlimited.

See additional restrictions described on inside pages

STINFO COPY

**AIR FORCE RESEARCH LABORATORY
PROPELLSION DIRECTORATE
WRIGHT-PATTERSON AIR FORCE BASE, OH 45433-7251
AIR FORCE MATERIEL COMMAND
UNITED STATES AIR FORCE**

NOTICE AND SIGNATURE PAGE

Using Government drawings, specifications, or other data included in this document for any purpose other than Government procurement does not in any way obligate the U.S. Government. The fact that the Government formulated or supplied the drawings, specifications, or other data does not license the holder or any other person or corporation; or convey any rights or permission to manufacture, use, or sell any patented invention that may relate to them.

This report was cleared for public release by the USAF 88th Air Base Wing (88 ABW) Public Affairs (AFRL/PA) Office and is available to the general public, including foreign nationals. Copies may be obtained from the Defense Technical Information Center (DTIC) (<http://www.dtic.mil>).

AFRL-RZ-WP-TR-2010-2073 HAS BEEN REVIEWED AND IS APPROVED FOR PUBLICATION IN ACCORDANCE WITH THE ASSIGNED DISTRIBUTION STATEMENT.

*/Signature//

JOHN HORWATH
Electrical Engineer
Mechanical Energy Conversion Branch
Power Division

//Signature//

JACK VONDRELL, Chief
Mechanical Energy Conversion Branch
Power Division
Propulsion Directorate

This report is published in the interest of scientific and technical information exchange, and its publication does not constitute the Government's approval or disapproval of its ideas or findings.

*Disseminated copies will show “//Signature//” stamped or typed above the signature blocks.

REPORT DOCUMENTATION PAGE

Form Approved
OMB No. 0704-0188

The public reporting burden for this collection of information is estimated to average 1 hour per response, including the time for reviewing instructions, searching existing data sources, gathering and maintaining the data needed, and completing and reviewing the collection of information. Send comments regarding this burden estimate or any other aspect of this collection of information, including suggestions for reducing this burden, to Department of Defense, Washington Headquarters Services, Directorate for Information Operations and Reports (0704-0188), 1215 Jefferson Davis Highway, Suite 1204, Arlington, VA 22202-4302. Respondents should be aware that notwithstanding any other provision of law, no person shall be subject to any penalty for failing to comply with a collection of information if it does not display a currently valid OMB control number. **PLEASE DO NOT RETURN YOUR FORM TO THE ABOVE ADDRESS.**

1. REPORT DATE (DD-MM-YY) March 2010			2. REPORT TYPE Final			3. DATES COVERED (From - To) 28 February 2007 – 28 December 2009		
4. TITLE AND SUBTITLE POWER AND THERMAL TECHNOLOGIES FOR AIR AND SPACE – SCIENTIFIC RESEARCH PROGRAM Delivery Order 0015: High Performance Permanent Magnets						5a. CONTRACT NUMBER FA8650-04-D-2403-0015		
						5b. GRANT NUMBER		
						5c. PROGRAM ELEMENT NUMBER 62203F		
6. AUTHOR(S) Christina Chen						5d. PROJECT NUMBER 3145		
						5e. TASK NUMBER SR		
						5f. WORK UNIT NUMBER 3145SR49		
7. PERFORMING ORGANIZATION NAME(S) AND ADDRESS(ES) University of Dayton Research Institute Metals and Ceramics Division, Magnetics Laboratory 300 College Park Dayton, OH 45469-0170						8. PERFORMING ORGANIZATION REPORT NUMBER UDR-TR-2009-00197		
9. SPONSORING/MONITORING AGENCY NAME(S) AND ADDRESS(ES) Air Force Research Laboratory Propulsion Directorate Wright-Patterson Air Force Base, OH 45433-7251 Air Force Materiel Command United States Air Force						10. SPONSORING/MONITORING AGENCY ACRONYM(S) AFRL/RZPG		
						11. SPONSORING/MONITORING AGENCY REPORT NUMBER(S) AFRL-RZ-WP-TR-2010-2073		
12. DISTRIBUTION/AVAILABILITY STATEMENT Approved for public release; distribution unlimited.								
13. SUPPLEMENTARY NOTES Report contains color. PA Case Number: 88ABW-2010-1012; Clearance Date: 08 Mar 2010.								
14. ABSTRACT Advanced permanent magnetic materials are in high demand by the Air Force. Developing high-performance nanomagnetic materials was the focus of this program. Methods for making anisotropic bulk nanocomposite magnets of Nd-Fe-B/Fe-Co, as well as Sm-Co/Co-Fe, were investigated, through which we gained comprehensive understanding in developing advanced magnetic nanocomposites. Several key challenges were identified, which include limiting oxidation during synthesis of the nanopowders, uniformly dispersing the two phases, maintaining the two distinct phases during consolidation processes at a limited temperature, and aligning the nanograins within the composite structure. Some possible solutions to overcome these challenges are recommended. Techniques of characterizing magnetic materials were also researched in this program by using both experiments and computer modeling, and the image effect in closed-circuit magnetic measurement was reported for the very first time by our researchers. The program also resulted in five published papers.								
15. SUBJECT TERMS permanent magnets, hard magnets								
16. SECURITY CLASSIFICATION OF:			17. LIMITATION OF ABSTRACT: SAR		18. NUMBER OF PAGES 50		19a. NAME OF RESPONSIBLE PERSON (Monitor) John Horwath	
a. REPORT Unclassified			b. ABSTRACT Unclassified		c. THIS PAGE Unclassified		19b. TELEPHONE NUMBER (Include Area Code) N/A	

Table of Contents

<u>Section</u>	<u>Page</u>
LIST OF FIGURES	iv
LIST OF TABLES	vi
GLOSSARY	vii
1. SUMMARY	1
2. INTRODUCTION	2
3. RESULTS AND DISCUSSION	3
3.1 Nano-Magnetic Materials of Nd-Fe-B and Fe-Co	3
3.2 Nanocomposite magnets of $\text{Sm}_2(\text{Co,Fe})_{17}$ and Fe-Co	8
3.3 Nanoparticles of Nd-Fe-B	13
3.4 Nanoparticles and bulk of PrCo_5 and SmCo_5	17
3.5 Magnetic Characterization In Closed-Circuit Measurements	21
3.5.1 The Phenomenon of Magnetization Distortion in Closed-Circuit Measurements	21
3.5.2 Analysis of the Distortion Using Computer Modeling	27
4. CONCLUSIONS AND RECOMMENDATIONS	33
4.1 Nanocomposite of Rare Earth Hard Phase and Fe-Co soft Phase	33
4.2 Nanoparticles of Rare Earth Permanent Magnetic Phases	33
4.3 Magnetic Characterization In Closed-Circuit	34
5. REFERENCES	35
APPENDIX – PUBLICATION LIST	37

LIST OF FIGURES

FIGURE	PAGE
1 H_{ci} vs. Pressing Temperature for the Magnets With and Without a Soft Phase Coating	4
2 H_{ci} vs. Deformation Temperature for the Magnets Made With Uncoated Powder	4
3 Specimen Made With Uncoated Powder Before (a) and After HP (b)	5
4 A Magnet (4% Fe-Co) After HP (580°C)	5
5 Fracture Surfaces After HP at 760°C	6
6 Fracture Surfaces of the Specimens (Uncoated) Deformed at 760°C (a) and 900°C (b)	6
7 Specimen With 4% Fe-Co After HD at 760°C	6
8 Fracture Surface of the Specimen Which is the Same as That Shown in Figure 7	7
9 SEM – BSE of the Specimen Which is the Same as That Shown in Figures 7 and 8	7
10 Partial Hysteresis Loops of $Sm(Co_{0.834}Fe_{0.166})_z$ With $z = 6.5-14.7$	9
11 Magnetic Properties of $Sm(Co_{0.834}Fe_{0.166})_z$ vs. Effective Z (28% Soft Phase for $z = 13$, and 35% Soft Phase for $z = 14.7$)	9
12 Magnetic Properties of $Sm(Co_{1-x}Fe_x)_{13}$ With 28% Soft Phase vs. Fe Content x	9
13 Effect of F Content on Magnetic Properties of $Sm[(Co_{0.7}Fe_{0.3})_{1-y}F_y]_{13}$ With $y = 0, 0.04$, and 0.08	10
14 TEM Microstructures of $Sm(Co_{0.73}Fe_{0.27})_{8.5}$ Compacted at 700°C With 10-100 nm Grain Sizes	11
15 SEM Micrograph of $Sm(Co_{0.834}Fe_{0.166})_{13}$ With 28% Co-Fe Soft Phases (a) Fracture Surface and (b - d) BSE Micrographs	11
16 EDS of $Sm(Co_{0.834}Fe_{0.166})_{13}$ Shown in Fig. 6: Black Area has 98% Co-Fe Plus 2% Sm; and the Matrix is $Sm(Co,Fe)_{8.2-10.6}$	12
17 Coercivity vs. Milling Time	14
18 TEM Micrographs of Nd-Fe-B Nanoparticles	15
19 SEM Microstructures of the Powders Milled for 30 Minutes	15
20 SEM Microstructures of the Powders Milled for 9 Hours	16
21 TEM Images of the Particles Suspended in the Solvent	18

LIST OF FIGURES (concluded)

FIGURE		PAGE
22	SEM Image of the Particles Sedimentated at the Bottom of the Solvent	18
23	SEM/EDS Results for the PrCo ₅ Powder and Bulk	18
24	Magnetization Curves of 4 Hours Milling PrCo ₅ Powder Epoxy Sample by VSM	19
25	XRD Patterns for PrCo ₅ Starting Powder, Milled 4 Hours Powder, and Bulk Pressed at 200°C	19
26	SEM Image of PrCo ₅ Bulk Compacted at 200°C	20
27	Effect of Pressing Temperature on the Coercivity and Density of PrCo ₅ Bulk	20
28	Magnetization Distortion in Closed-Circuit Testing of Nd-Fe-B Magnets With Different <i>L/D</i> Values	21
29	Setup of Closed-Circuit Magnetic Measurement for Both Measurements	23
30	Magnetization Distortion in Closed-Circuit Testing of 1018 Steel With Different <i>L/D</i>	24
31	Magnetization Curves for Four Materials With <i>L/D</i> = 0.30 (<i>L</i> = 0.377 cm) Tested in Closed-Circuit	24
32	Magnetization $4\pi M$ vs. Magnetic Field for Four Materials	25
33	Magnetic Induction <i>B</i> vs. Magnetic Field for Four Materials	25
34	Decreased Values of $4\pi M$ and <i>H</i> vs. Maximum Measured Magnetization	26
35	Calculated Field Distribution in Closed-Circuit Testing of 1018 Steel Samples	28
36	Calculated Magnetic Field Values vs. Radial Position With Varying <i>L/D</i>	28
37	Calculated Magnetic Field Values vs. Radial Position Along the Midplane Through the Samples With Varying <i>L/D</i>	29
38	Calculated Distribution of Flux Density <i>B</i> in Closed-Circuit Testing of 1018 Steel Samples	30
39	Calculated Field <i>H</i> Along Lines Parallel to the Magnet/Sample Axis for the Sample With <i>L/D</i> = 0.23	30
40	As Fig. 37, for Sample with <i>L/D</i> = 1.8	31
41	Calculated Flux Density <i>B</i> Along Lines Parallel to the Sample/Magnet Axis for the Sample with <i>L/D</i> =0.23	31
42	As Fig. 41, for Sample With <i>L/D</i> =1.8	32

LIST OF TABLES

TABLE		PAGE
1	Intrinsic Magnetic Properties of Selected R-Fe and R-Co Compounds	2
2	Grain Size and Coercivity vs. Process Temperature	5
3	Details of the High Energy Milling Using Spex-8000	13
4	Grain Size Estimated from XRD Patterns by Software	16
5	Magnetic Fields and Inductions Obtained in Closed-Circuit Measurement	26
6	Magnetization Obtained in Closed-Circuit Measurement	26

LIST OF ACRONYMS, ABBREVIATIONS, AND SYMBOLS

ACRONYM	DESCRIPTION
$4\pi M$	Magnetization
$(BH)_{\max}$	Maximum energy product
EDS	Energy-dispersive X-ray spectroscopy analysis
H_{ci}	Intrinsic coercivity
HD	Hot deformation
HP	Hot pressing
MDC	Magnetic dynamic compaction
PVD	Plasma vapor deposition
SAXS	Small angle X-ray scattering
SEM	Scanning electron microscope
TEM	Transmission electron microscope
VSM	Vibrating sample magnetometer
XRD	X-ray diffraction

1.0 SUMMARY

High performance permanent magnets were the focus of our efforts in this program, and research efforts on the techniques characterizing the magnetic materials has also been made. Under this AFRL contract, research on the following five topics has been conducted:

1. Nanocomposite magnets of Nd-Fe-B and Fe-Co
2. Nanocomposite magnets of $\text{Sm}_2(\text{Co}_{1-x-y}\text{Fe}_x\text{M}_y)_{17}$ and Co-Fe
3. Nanoparticles of Nd-Fe-B
4. Nanoparticles and bulk of PrCo_5 and SmCo_5
5. Magnetic characterization technology – Magnetization distortion in closed-circuit measurement and analyses using computer modeling.

Development of anisotropic bulk nanocomposite of Nd-Fe-B and Fe-Co, as well as Sm-Co and Co-Fe, has been extensively experimented in this program. Throughout our efforts since February 2007, we have revealed various facts about the nano-magnetic materials and the nanotechnology needed to make them, and have gained comprehensive understanding in developing the advanced nanocomposites of magnetic materials. Several key challenges have been identified which include limiting oxidation during synthesizing the nanopowders, uniformly dispersing the two phases, maintaining the two distinct phases during consolidation processes at elevated temperature, and aligning the nanograins within the composite structure. Some possible solutions to overcome those challenges have been suggested for the next steps.

Nanotechnology for producing nanocomposite magnets includes two different routines: the “Top-down” routine that starts from the micro-size powders consisted of nanograins, and the “Bottom-up” routine that starts from the nanoparticles. During the first two years, the “Top-down” routine was used for our research. The “Bottom-up” routine was employed in the third year of this program after the “Top-down” routine faced challenges which could not be solved using current technology. SmCo_5 and PrCo_5 nanoparticles have been successfully synthesized using surfactant-assisted high energy ball milling. Nd-Fe-B nanoparticles with reasonable coercivity have yet to be synthesized. Research to make the anisotropic bulks with full density is still in progress.

During the research process, we also studied the magnetic characterization techniques, reported the phenomenon and the analyses results of magnetization distortion in the first and third quadrants in closed-circuit magnetic measurement, which was the very first report on this phenomenon and its research.

During 2008-2009, as the results of this program, we published five papers in the *J. of Applied Physics*, *IEEE Transaction on Magnetics*, and the *J. of Magnetism and Magnetic Materials*, etc. We also co-authored seven papers with some researchers in other groups. Recently we submitted two more papers for publications, and are hopeful these two papers will be published in 2010. The details are listed in the Appendix.

2.0 INTRODUCTION

High-energy permanent magnets are of great demand for both commercial and military applications. Bulk magnets are important functional components in electric machines including PM motors, generators used for green energy, hybrid/electrical vehicles, military airplanes, power electronics, electric drive and propulsion, traveling microwave tubes, and magnetic bearings in high temperature for jet engines and other applications.

The concept of nanocomposite magnets consisting of a magnetic hard phase and a soft phase is theoretically applicable, which would take advantage of the two distinct phases to generate a significantly higher energy product. The performance of permanent magnetic devices and machines is ultimately limited by the maximum energy product $(BH)_{max}$ and the maximum operating temperature of the available materials. The $(BH)_{max}$ achieved in the sintered Nd-Fe-B magnets exceeds 59 MGoe [1] almost reaching the theoretical limit for the $Nd_2Fe_{14}B$ compound, 64 MGoe. The latter value, in its turn, is the highest among presently known high-anisotropy magnetic compounds as shown in Table 1 [2-4]. Therefore, unless a novel, superior compound is discovered, the further progress in permanent magnets can be sought through combining the high-anisotropy magnetic materials with high-magnetization soft magnetic materials. The phenomenon which makes it possible to combine such different materials is based on in magnetic exchange coupling between the adjacent grains of two magnetic phases caused by a short-range exchange interaction [5-6].

On the other aspect, Sm-Co 1:5 or 2:17 magnets with $\sim 30\%$ lower $(BH)_{max}$ have the best thermal stability among all permanent magnetic materials [7]. For applications at elevated temperatures, especially for the Air Force's application, thermal stability is highly desired.

Therefore, this research efforts in this program focused on developing nanocomposites with Nd-Fe-B and Sm-Co as the hard phases and Fe-Co as the soft phase. Our efforts also included research on magnetic characterization technology, which engages understanding the basics of the magnetic phenomenon and improving the precision of the magnetic measurements.

Table 1. Intrinsic Magnetic Properties of Selected R-Fe and R-Co Compounds

Compound	$4\pi M_s$ (kG)	T_c (°C)	H_A (kOe)	Candidate as a Hard Phase in Nanocomposite	Ref.
$Nd_2Fe_{14}B$	16.0	310	75	Good	2
$Pr_2Fe_{14}B$	15.6	300	75	Good	2
$Sm_2Fe_{14}B$	15.0	345	very small	No Good	2
$PrCo_5$	12.0	620	170	Good	3
$SmCo_5$	11.4	727	250	Good	3
YCo_5	10.6	630	130	Maybe	3
Nd_2Co_{17}	13.9	890	very small	No Good	3
Sm_2Co_{17}	12.5	920	65	Good	3
$Sm_2(Co_{0.7}Fe_{0.3})_{17}$	14.5	840	52	Good	3
Pr_2Co_{17}	13.8	880	very small	No Good	4
$Pr_2(Co_{0.6}Fe_{0.4})_{17}$	16.0	760	15	May not	4
Y_2Co_{17}	12.8	930	very small	No Good	3

3.0 RESULTS AND DISCUSSION

3.1 Nano-magnetic Materials of Nd-Fe-B and Fe-Co

Using hot-deformation (HD) after hot-pressing (HP) can produce bulk nanostructured composites with an energy product $(BH)_{max}$ of 48-55 MGOe, made of melt spun Nd-Fe-B powder coated with Fe or Fe-Co soft-phase [8-10]. However, these methods have not resulted in further improvement in $(BH)_{max}$. The major obstacles to producing high performance include the following: (1) an intolerable oxygen content, which is associated with finer particle size of the rare earth hard phase for uniformly dispersing the hard and soft phases, affects the coercivity significantly; (2) a high process temperature, which is required for achieving sufficient density and alignment, reduces the coercivity of the magnets, especially those with a large volume of the soft-phase. Our efforts in this project included determining the effects of the process temperature on the coercivity, and looking for possible solutions to overcome the difficulties.

Specimens with and without magnetic soft phase were compacted in vacuum at 11 designated temperatures from 25 to 760°C for 2 minutes. All the specimens weighed 5 to 12 g each. The specimens without a soft phase were made with pre-crystallized Nd-Fe-B ribbon powder having composition of $Nd_{13.5}Fe_{bal}Co_{6.7}Ga_{0.5}B_6$ and grain size of less than 40 nm. The specimens with a soft phase were made using the same Nd-Fe-B powder, but electro-coated with Fe-Co. A large particle size (100 to 150 μm) was selected for the Nd-Fe-B to minimize the oxidation effect, and small volumes ($\leq 4\%$) of the soft-phase coating were used to avoid a thick coating layer, which would result in decoupling. A larger volume of Fe (~8%) coated by PVD (Plasma vapor deposition) was also studied. The coating percentages were determined by calibrating the saturation magnetization, $4\pi M_s$, of the isotropic specimens with those of the magnets made with and without blended Fe powder. Some specimens were also deformed with 70% length deduction at $T = 640$ to 900°C. The oxygen contents for all the magnets were controlled at ≤ 0.18 wt%. A KJS-HG700 hysteresigraph was used to test magnetic properties, and a scanning electron microscope (SEM) was used for characterizing microstructure.

Two major effects of process temperature that reduce coercivity H_{ci} can be observed from Figure 1, showing H_{ci} vs. pressing temperature. The first is the grain-growth effect at $T > 620^\circ C$ for the magnets without a soft-phase coating, and it is profound at $T > 660^\circ C$ where the H_{ci} decreases sharply. The peak H_{ci} at 550-610°C indicates the occurrence of full crystallization. The second is the soft phase effect, which occurs at $T \geq 300^\circ C$. The H_{ci} decreases monotonically from 17 kOe at 300°C to 3.7 kOe at 760°C.

Figure 2 shows H_{ci} vs. deformation temperature for the magnets without a coated soft phase. As the temperature rises, the H_{ci} decreases slightly at $T \leq 780^\circ C$ and reduces rapidly at $T \geq 820^\circ C$. Table 2 lists the grain sizes and magnetic properties after processing at various temperatures. Three processes are listed as pressing, HP, and HD. Figure 3 shows the SEM microstructures of the specimens before and after HP at 580°C. Figures 4 through 9 show the SEM microstructures of the specimens made with and without Fe-Co coating after HP at 580°C and 760°C and HD at 760°C and 900°C.

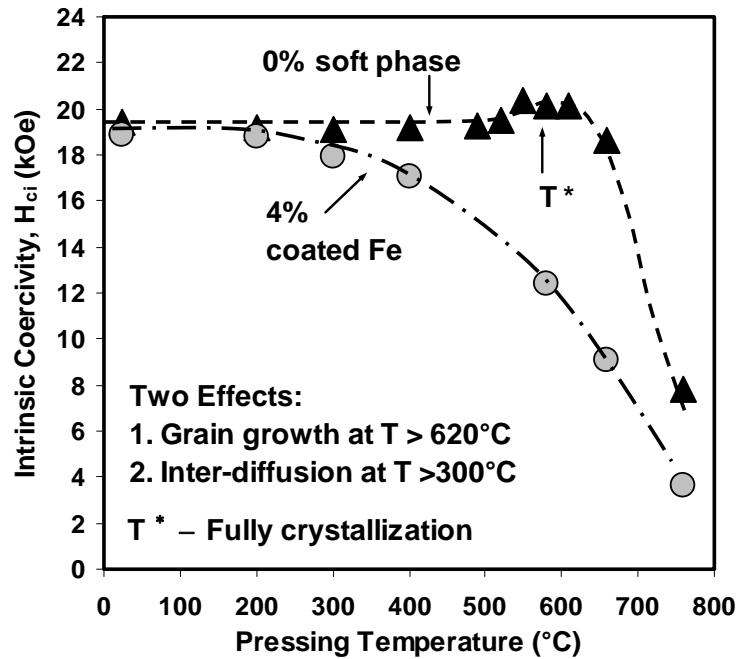


Figure 1: H_{ci} vs. Pressing Temperature for the Magnets with and without a Soft Phase Coating

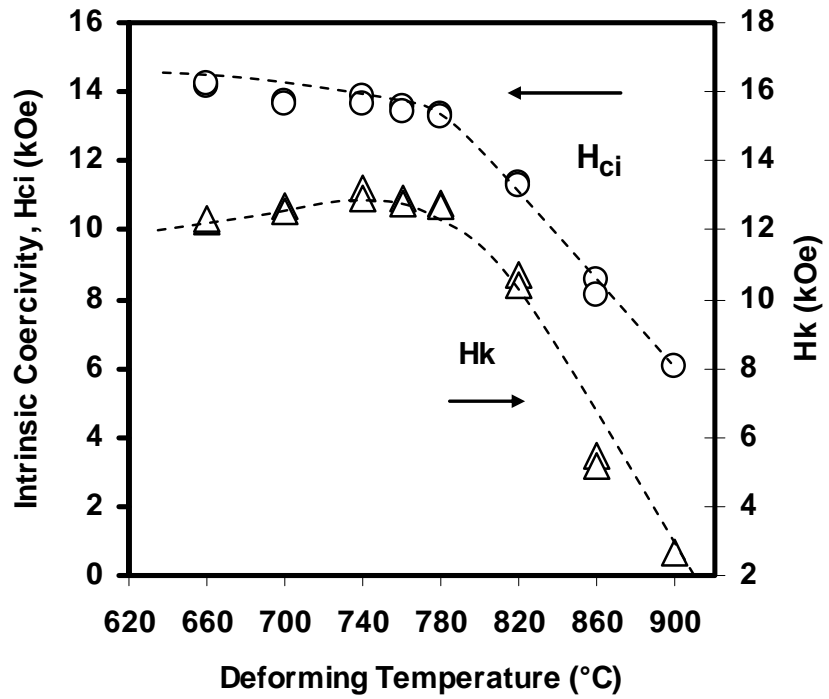


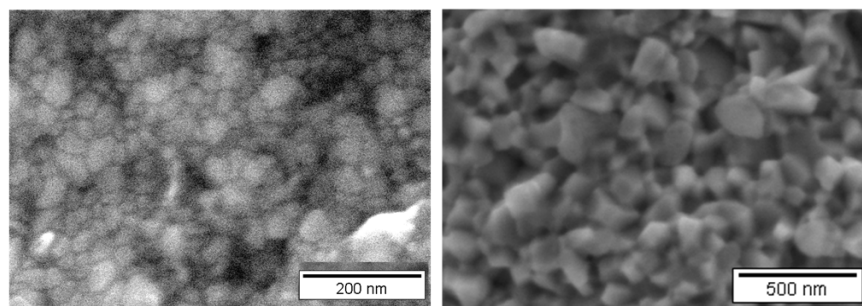
Figure 2: H_{ci} vs. Deformation Temperature for the Magnets made with Uncoated Powder

Table 2. Grain Size and Coercivity vs. Process Temperature

Process	Temp. (°C)	Grain Size (nm)	H _{ci} (kOe) at various Fe-Co%				(BH) _{max} (MGOe) at various Fe-Co%			
			0%	~ 1%	~ 4%	~ 8%♦	0%	~ 1%	~ 4%	~ 8%♦
Pressing	25	< 40	19.3		19.0		15.6		15.7	
Hot-Press (HP)	400	< 40	19.4		17.1		15.4		13.9	
	580	~40 – 100	20.1	19.5	12.3	13.1	15.5	15.9	13.7	14.1
	760	~300 – 1500	7.8		3.7		10.7		6.0	
HD after HP at 580°C	760	~(40 - 100) //, ~(200 - 800) ⊥*	14.1	12.5	3.6	2.7	48.2	51.3	31.3	15.7
	900	~(60 – 200) ///* ~(300–1500) ⊥	6.0				17.8			

* // is along the pressure direction and ⊥ is perpendicular to the pressure direction

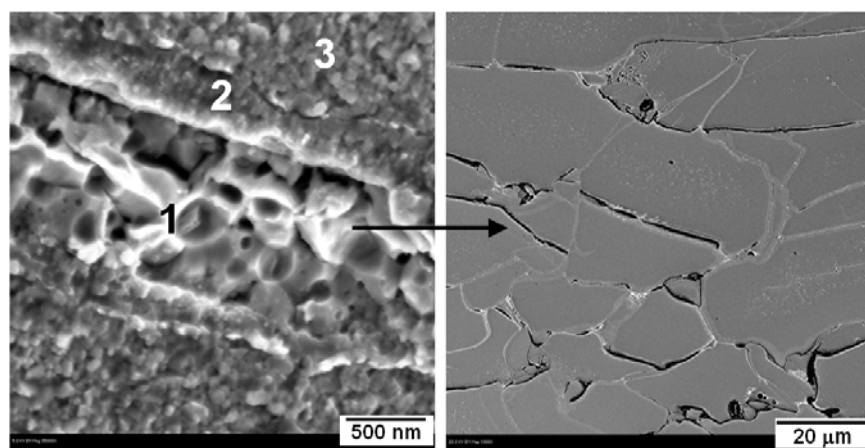
♦ Coated with Fe using PVD



(a) Powder before HP

(b) Fracture surface after HP at 580°C

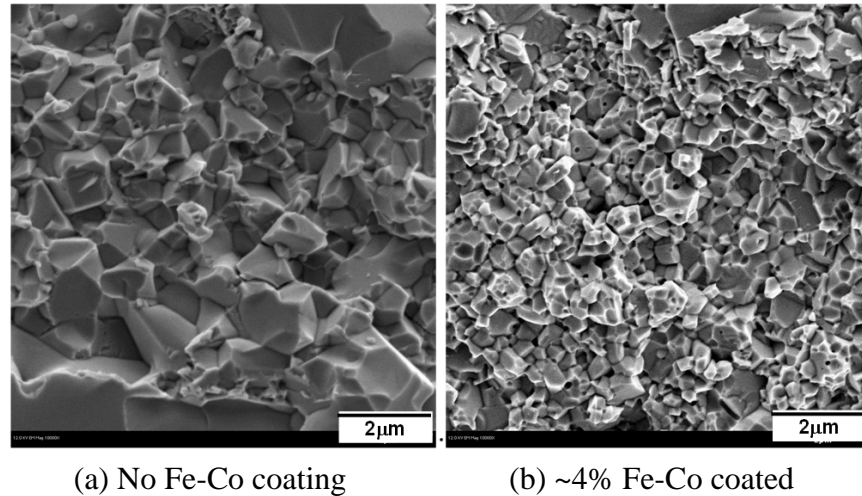
Figure 3: Specimen made with uncoated powder before (a) and after HP (b)



(a) Fracture surface

(b) BSE micrograph

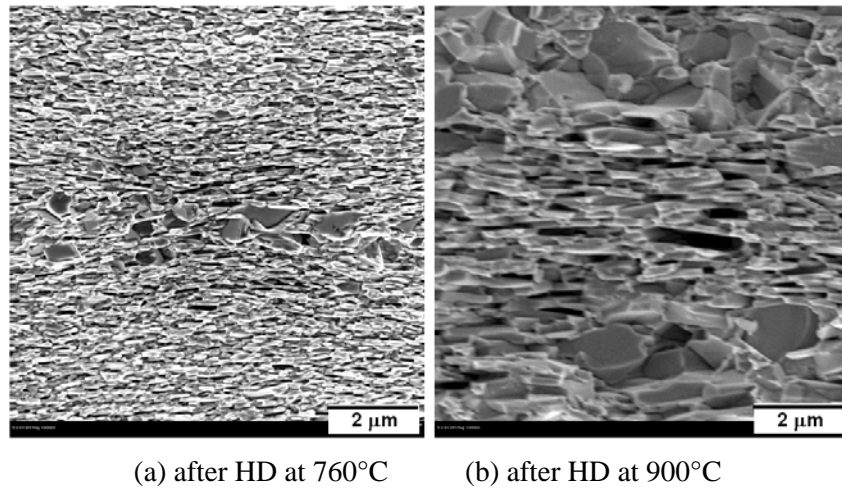
Figure 4: A magnet (4% Fe-Co) after HP at 580°C: 1. Fe-Co, 2. Diffusion zone, and 3. Nd-Fe-B



(a) No Fe-Co coating

(b) ~4% Fe-Co coated

Figure 5: Fracture Surfaces after HP at 760°C: (a) without and (b) with Soft Phase



(a) after HD at 760°C

(b) after HD at 900°C

Figure 6: Fracture Surfaces of the Specimens (Uncoated) Deformed at 760°C (a) and 900°C (b)

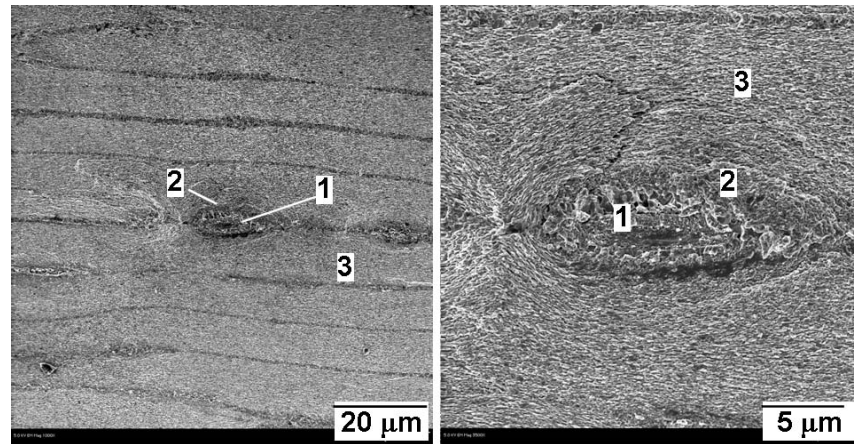


Figure 7: Specimen with 4% Fe-Co after HD at 760°C:

1. Fe-Co, 2. Diffusion Layer, and 3. Nd-Fe-B

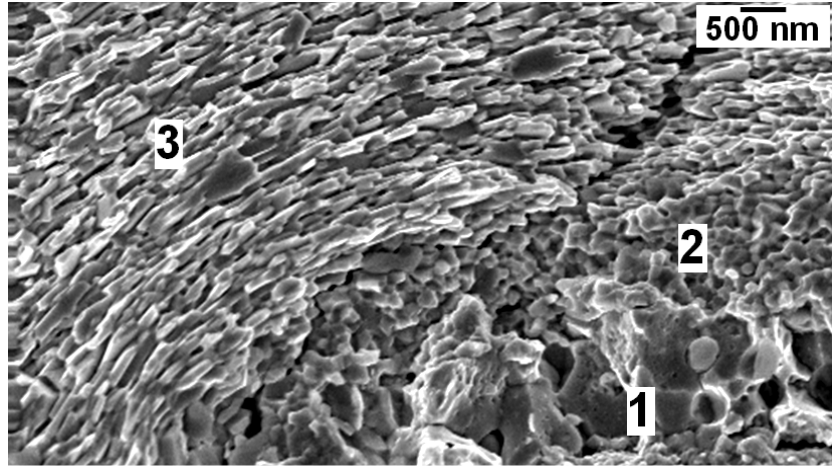


Figure 8: Fracture Surface of the Specimen which is the Same as That Shown in Fig. 7

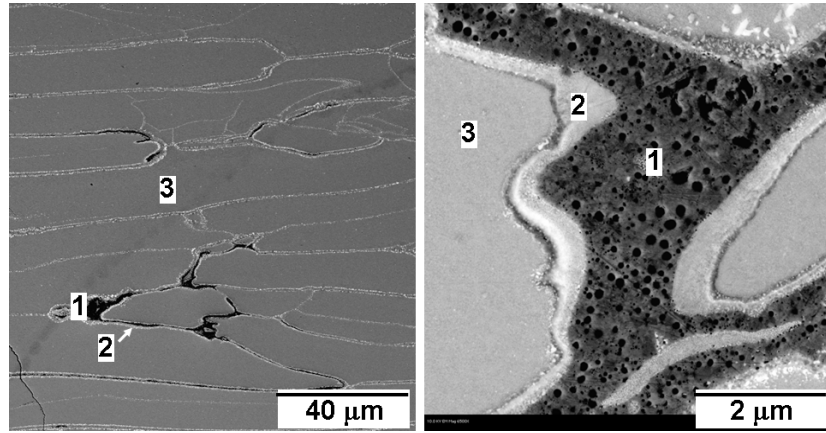


Figure 9: SEM – BSE of the Specimen which is the Same as That Shown in Figures 7 & 8

In summary, we find the following:

- For the magnets made with uncoated Nd-Fe-B powder, grain-growth effect on coercivity plays a dominant role when $T > 610^{\circ}\text{C}$. HP at 580°C resulted in grain size of 40-100 nm and $H_{ci} = 20.1$ kOe. HP at 760°C resulted in grain size of 300-1500 nm and $H_{ci} = 7.8$ kOe.
- Compared to the magnets without the Fe-Co soft phase, the magnets with 4% coated Fe-Co has 10% lower H_{ci} after HP at 300°C and 81% lower H_{ci} after HP at 760°C . Interdiffusion between the hard phase and the soft phase is the major reason for coercivity reduction.
- The processing methods significantly affect the grain morphology and coercivity. For the same process temperature 760°C , the Nd-Fe-B hard phase has large equal-axial grains up to 1500 nm and $H_{ci} = 7.8$ kOe if it was pressed, and it has plate-shape grains up to 100 x 800 nm with $H_{ci} = 14.1$ kOe if it was deformed.
- To obtain a high coercivity that is required for a high energy product, the process temperature must be less than 300°C that would retain two distinct phases.

3.2 Nanocomposite Magnets of $\text{Sm}_2(\text{Co, Fe, M})_{17}$ and Fe-Co

Nanocrystalline $\text{Sm}(\text{Co, Fe})_z$ magnets with $z = 5$ to 8.5 made using mechanical alloying have been reported since 1991 [11-14]. High-energy milling followed by devitrification forms a uniform nanocrystalline structure leading to good isotropic hard magnetic properties. These materials with $z = 5$ to 8.5 mostly include 1:5 phase, 2:17 phase, and other phases in between the 1:5 and 2:17. The intention of this investigation is to explore the alloys of $\text{Sm}(\text{Co, Fe, M})_z$ with $z > 8.5$, which would involve a nanocomposite of the 2:17 hard phase and Fe-Co soft phase, or possible new phases formed with some additive elements. This investigation also searches for new techniques that may provide the ability to make effective exchange coupled nanocomposites of $\text{Sm}_2(\text{Co, Fe})_{17}$ hard phase and Fe-Co soft phase with anisotropic magnetic properties.

Bulk nanocrystalline magnets were made using mechanical alloying and hot compaction with compositions of $\text{Sm}(\text{Co}_{1-x}\text{Fe}_x)_z$ with $z = 5.6$ to 14.7 and $\text{Sm}[(\text{Co}_{1-x}\text{Fe}_x)_{1-y}\text{F}_y]_z$ with $x = 0$ to 0.575, $y \leq 0.08$ (or $\text{F} \leq 2.0$ wt%), and $z = 6.5$ to 13. A SPEX-8000 high energy mill was used to make amorphous powder from mixtures of several melted base alloys. All the alloys were made using an arc melting furnace with Sm (99.95%), and Fe and Co metals (99.99%). The fluorine inclusion for some specimens was added using CoF_2 powder (98%). The milling time was 16 hours in order to obtain the amorphous state for majority powder particles, which was verified using x-ray diffraction (XRD). The amorphous powders were then compacted under pressure of 25 kpsi with vacuum pressure better than 10^{-5} Torr. The pressing temperature was in the range of 700 to 750°C, depending on the Fe and Sm contents. Higher Fe and Sm contents require a lower compacting temperature to crystallize the amorphous powder and obtain a full density, which was in the range of 8.0 to 8.5 g/cm³. Each specimen weighed 5 to 8 grams. Oxygen contents in the range of 0.25 to 0.35 wt% were tested using LECO equipment. All the “z” values are the effective “z” determined by using the nominal Sm deducting the Sm, which reacted with 0.30 wt% oxygen. A KJS hysteresigraph was used to characterize the magnetic property and SEM with energy dispersive spectroscopy (EDS) as well as transmission electron microscope (TEM) were used for microstructure characterization.

a) Magnetic Properties

Partial hysteresis loops for the $\text{Sm}(\text{Co}_{0.834}\text{Fe}_{0.167})_z$ magnets with $z = 5.6$ to 14.7 are shown in Fig. 10, and the magnetic properties for these magnets are shown in Fig. 11. The “z” effect on coercivity H_{ci} is obvious in these two figures. Although the H_{ci} decreased from 12 kOe at $z = 6$ to 3.3 kOe at $z = 14.7$, the H_{ci} value is considerably good for such large “z”, showing evidence of exchange coupling between the hard phase of $\text{Sm}_2(\text{Co, Fe})_{17}$ with $z = 8.5$ and the soft phase of Co-Fe. The H_{ci} is 8.4 kOe at $z = 8.5$ and 4.2 kOe at $z = 13$. Energy products $(\text{BH})_{\text{max}}$ ranging from 4.2 to 12.2 MGOe were obtained for these nanocrystalline magnets.

The magnetic properties of $\text{Sm}(\text{Co}_{1-x}\text{Fe}_x)_{13}$ series with $x = 0$ to 0.575 are shown in Fig. 12. The H_{ci} values for the series of $\text{Sm}(\text{Co}_{1-x}\text{Fe}_x)_{13}$ are 4.6 kOe at $x = 0.1$, and 2.2 kOe at $x = 0.55$. Zero Fe content does not result in the highest coercivity. Other series, including $\text{Sm}(\text{Co}_{1-x}\text{Fe}_x)_{8.5}$, were also studied, and the highest $(\text{BH})_{\text{max}}$ value obtained was 13.8 MGOe for bulk nanocrystalline $\text{Sm}(\text{Co}_{0.75}\text{Fe}_{0.23})_{8.5}$ magnet.

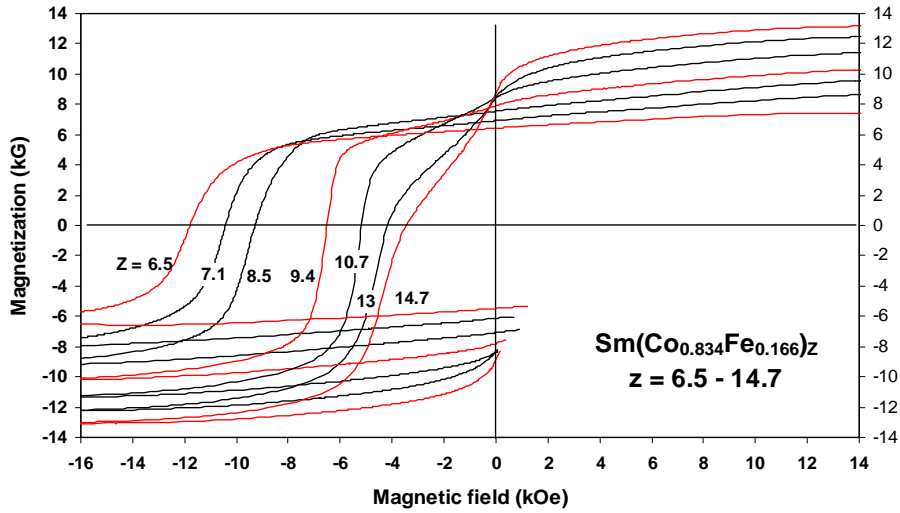


Figure 10: Partial Hysteresis Loops of $\text{Sm}(\text{Co}_{0.834}\text{Fe}_{0.166})_z$ with $z = 6.5\text{--}14.7$

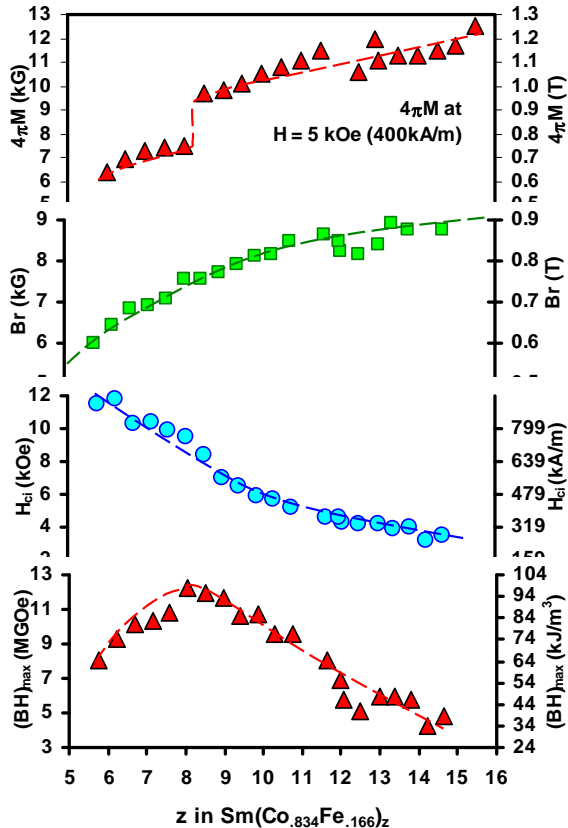


Figure 11: Magnetic properties of $\text{Sm}(\text{Co}_{0.834}\text{Fe}_{0.166})_z$ vs. z (28% Soft Phase for $z = 13$, and 35% Soft Phase for $z = 14.7$)

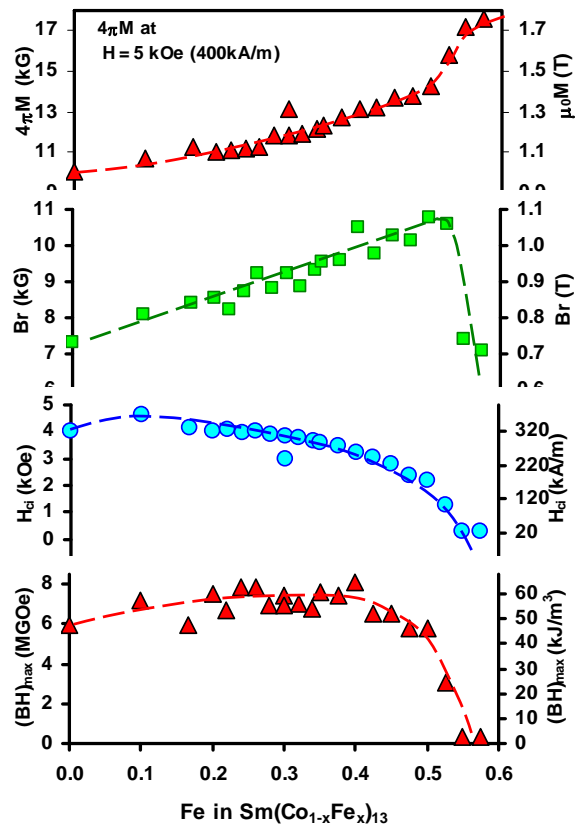


Figure 12: Magnetic Properties of $\text{Sm}(\text{Co}_{1-x}\text{Fe}_x)_{13}$ with 28% Soft phase vs. Fe Content x

Figure 13 shows the effect of fluorine on the magnetic properties of $[Sm(Co_{0.7}Fe_{0.3})_{1-y}F_y]_z$ with $y = 0, 0.04$ and 0.08 and $z = 6.5, 7.6, 8.5$ and 13 . As the figure shows, both saturation magnetization $4\pi M_s$ and magnetic remanence B_r increase slightly when F content y increases from 0 to 0.04 , indicating some degree of texture attributed to a small amount of F.

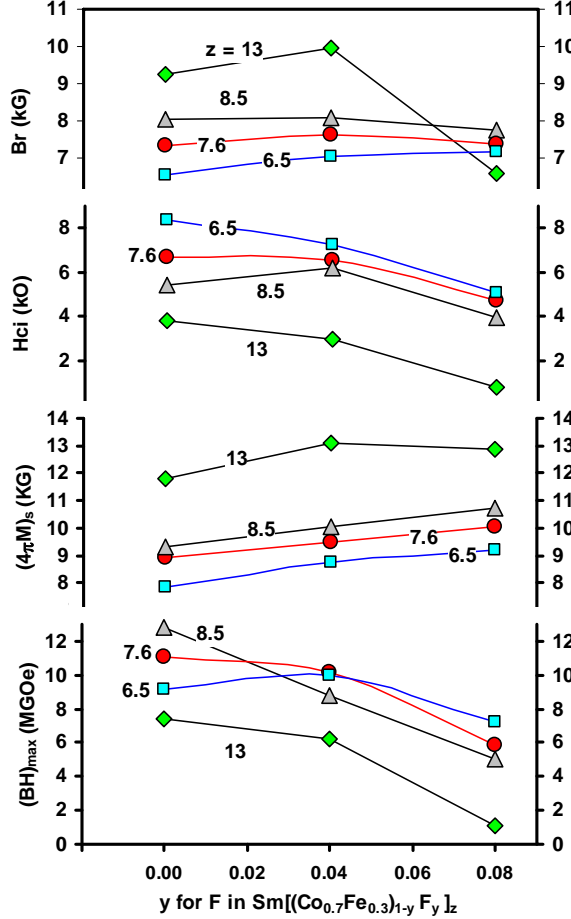


Figure 13: Effect of F Content on Magnetic Properties of $Sm[(Co_{0.7}Fe_{0.3})_{1-y} F_y]_{13}$ with $y = 0, 0.04$, and 0.08

b) Microstructures and Phases

Figure 14 shows a TEM microstructure of $Sm(Co_{0.73}Fe_{0.27})_{8.5}$ compacted at $700^\circ C$ that has $(BH)_{max} = 13.8$ MGoe and $H_{ci} = 7.4$ kOe. The grain size is in the range of 10 to 100 nm.

Figure 15 shows SEM microstructures of $Sm(Co_{0.834}Fe_{0.166})_{13}$ compacted at $750^\circ C$. The fracture surface in Fig. 6a shows the grain size is 40 to 300 nm. The SEM-BSE images in Figs. 6b to 6d show the matrix and a black phase. As shown in Fig. 16, the black phase is Co-Fe, and the matrix is Sm-Co (2:17) phase with Th_2Ni_{17} crystal unit, which was determined by using XRD. The dispersed dots of Co-Fe black phase have grain size in the range of 20 to 150 nm, and some areas of the Co-Fe black phase have grain size >200 nm. According to the calculation, $Sm(Co_{0.834}Fe_{0.166})_{13}$ has 28% soft phase, and $Sm(Co_{0.834}Fe_{0.166})_{14.7}$ has 35% soft phase.

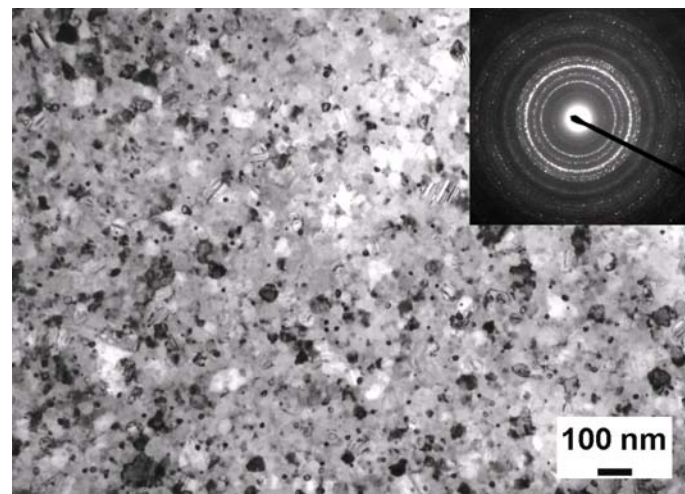


Figure 14: TEM microstructures of $\text{Sm}(\text{Co}_{0.73}\text{Fe}_{0.27})_{8.5}$ compacted at 700°C

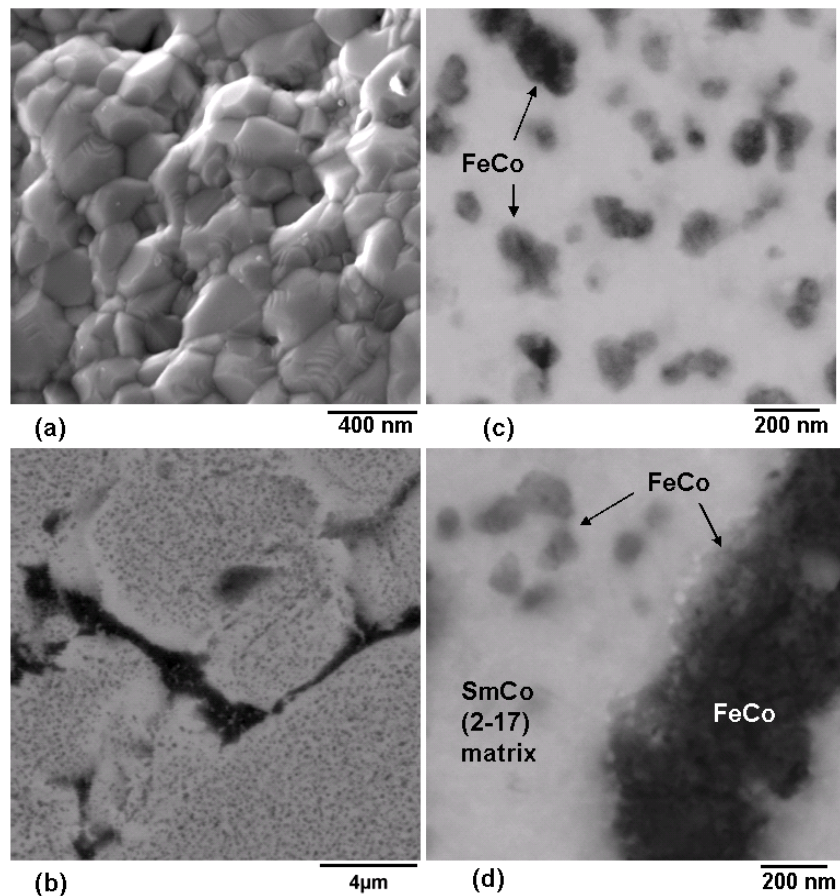


Figure 15: SEM micrograph of $\text{Sm}(\text{Co}_{0.834}\text{Fe}_{0.166})_{13}$ with 28% Co-Fe Soft Phases:
(a) Fracture Surface and (b - d) BSE Micrographs

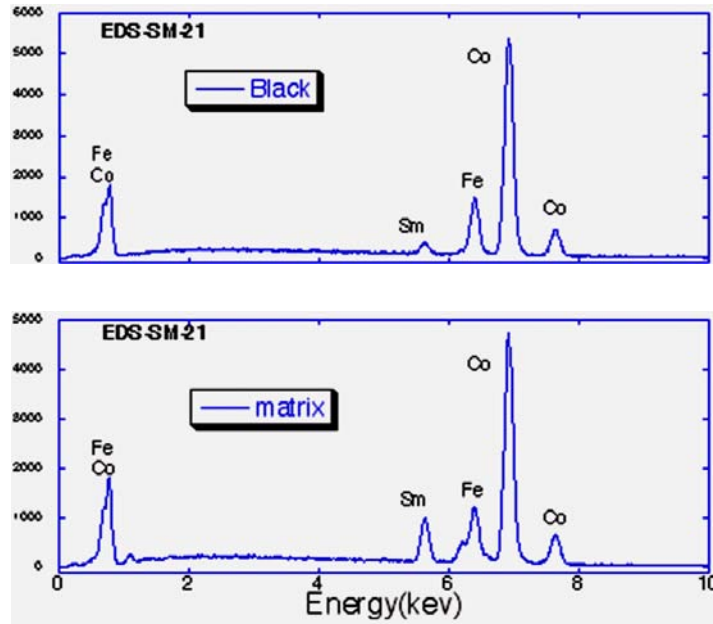


Figure 16: EDS of $\text{Sm}(\text{Co}_{0.834}\text{Fe}_{0.166})_{13}$ Shown in Fig. 6:
Black Area Has 98% Co-Fe plus 2% Sm; and the Matrix is $\text{Sm}(\text{Co},\text{Fe})_{8.2-10.6}$

Bulk nanocrystalline magnets can be made using mechanical alloying and hot compaction, whose compositions were $\text{Sm}(\text{Co}_{1-x}\text{Fe}_x)_z$ and $\text{Sm}[(\text{Co}_{1-x}\text{Fe}_x)_{1-y}\text{F}_y]_z$ with $z = 5.6$ to 14.7 , $x = 0$ to 0.575 , and $y = 0$ to 0.08 . The remanence B_r of isotropic $\text{Sm}(\text{Co}_{0.834}\text{Fe}_{0.167})_z$ increases from 6.0 to 9.1 kG as “z” increases from 5.6 to 14.7 . Although the coercivity H_{ci} decreased from 12 kOe at $z = 6$ to 3.3 kOe at $z = 14.7$, the H_{ci} is noticeably good for such large “z” or large percentage of Fe-Co phase, showing evidence of exchange coupling, since the magnet with $z = 14.7$ has 35% Fe-Co and 65% $\text{Sm}_2(\text{Co},\text{Fe})_{17}$. The H_{ci} for the series of $\text{Sm}(\text{Co}_{1-x}\text{Fe}_x)_{13}$ is 4.6 kOe at $x = 0.1$, and 2.2 kOe at $x = 0.55$. The energy product $(\text{BH})_{\text{max}}$ ranging from 3.0 to 13.8 MGOe was obtained for these magnets. Magnets of $\text{Sm}[(\text{Co}_{1-x}\text{Fe}_x)_{1-y}\text{F}_y]_z$ series show some increase in saturation magnetization $4\pi M_s$ and $(\text{BH})_{\text{max}}$ for the magnets with $y = 0.04$ and $z < 7.6$, seeming to be a sign of texture forming during compaction.

TEM and SEM/EDS analyses show the SmCo 2:17 hard phase and Fe-Co soft phase co-existing in the specimens with $z > 8.5$. Although the coercivity H_{ci} decreased as z increases, the H_{ci} is noticeably good for such large “z” or large percentage of Fe-Co soft phase. According to the calculation, the magnet of $z = 13$ with 28% soft phase has $H_{ci} = 4.2$, and the magnet of $z = 14.7$ with 35% soft phase has $H_{ci} = 3.3$ kOe.

It is our hope that the nanotechnologies would lead to discover new phases with $(\text{BH})_{\text{max}} > 60$ MGOe. One of these new phases may have compositions near $\text{Sm}(\text{Co},\text{Fe})_{13-16}$ with $4\pi M_s > 16$ kG and $H_{ci} > 10$ kOe, which may be obtained by modifying the crystal unit cell or the distance between the Sm and Co-Fe atoms in crystal cells. Fluorine inclusion was just one of the attempts, which did not show promising results.

3.3 Nanoparticles of Nd-Fe-B

As described in the previous sections, the developments of anisotropic bulk nanocomposite of Nd-Fe-B and Fe-Co, as well as Sm-Co and Co-Fe, had been extensively experimented using the “Top-down” routine since the beginning of the program. Throughout our efforts, we have realized that there are several key challenges preventing us to achieve our goals which could not be solved by using current techniques. In this case, the “Bottom-up” routine, starting from synthesizing nanoparticles, was employed in the third year of this program.

The “Top-down” routine starts from micro-size powders containing nanograins, and the “Bottom-up” routine starts from making nanoparticles. Making Nd-Fe-B nanoparticles with useful coercivity has been a challenge for research groups in our field world wide [15-16]. A Texas based group, with Prof. J. Ping Liu, has been trying to make the Nd-Fe-B nanoparticles for years without much success in spite of their successes in synthesizing PtFe and SmCo nanoparticles [19-22].

The reasons for making Nd-Fe-B nanoparticles include the fact that we had extensive experience on high energy milling.

Attempts to synthesize Nd-Fe-B nanoparticles was made using surfactant-assistant high energy milling with various milling times (0.5, 1.5, 3, 6 and 9 hours). The details for the milling condition are shown in Table 3. In order to prevent oxidation, all the loadings and unloading were done in an Ar dry-box. The powders were then dried in vacuum and magnetic aligned in uncured epoxy. The samples were then held in between permanent magnets during the epoxy curing period.

Table 3. Details of the High Energy Milling Using Spex-8000

ID / milling time / g	Milling Materials	wt.%	wt (g)	Note
NNd2A / 0.5 hr / ~1	Crystallized Nd-Fe-B (F2) Ribbon powder (300 – 400 μ m)	50.00	15	Magnetic material
NNd2B / 1.5 hr / ~1	Menhaden fish oil, blown Z-3 (containing non-oxygen agents)	2.33	0.7	Dispersant (surfactant)
NNd2C / 3.0 hr / ~1	Xylenes (C_8H_{10})	14.33	4.3	Solvent
NNd2D / 6.0 hr / ~1	Heptanes (C_7H_{16})	33.33	10	Solvent
NNd2E / 9.0 hr / ~9	3/16" Steel balls: 20.1 g (46 pcs)	N/A		Milling energy
	Total	100	30	

Magnetic characterization was done using a hysteresigraph, and the effect of milling time on the coercivity is shown in Fig. 17. The coercivity of the particles decreases as the milling time increases which is not what we expected to see. Since the particles were always protected

by the surfactant containing non-oxygen agents, oxidation should be minimized. We believe that a longer high energy milling time resulted in many crystal defects, such as dislocations in the crystal lattice caused by mechanical stress and strain, which made the coercivity decrease significantly. A longer milling time results in less perfect crystal lattice, especially for Nd-Fe-B phase since it has higher toughness compared to Sm-Co phases. (This is the reason that Nd-Fe-B can be deformed at 600 to 800°C to form alignment, and SmCo cannot be aligned by deformation).

Amorphous metal does not have any anisotropy and coercivity, and less perfect crystal lattice would have lower coercivity. Unlike the mechanical alloyed powder which going through re-crystallization during hot compaction, the surfactant-assistant high energy milled powder did not go through a re-crystallizing step.

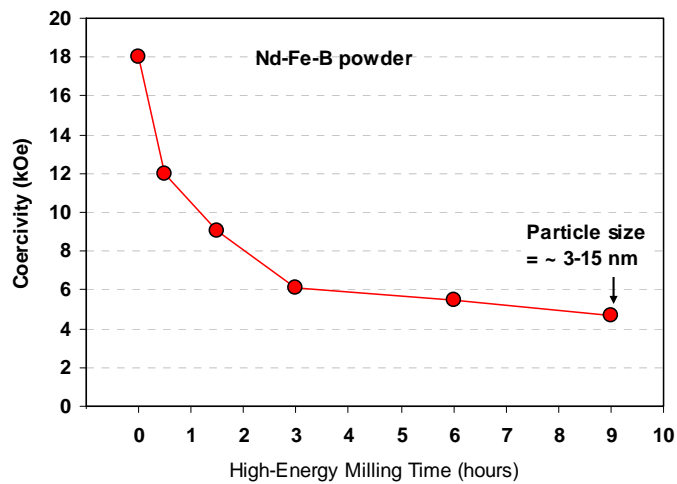


Figure 17. Coercivity vs. Milling Time

The Nd-Fe-B powder after 9 hours of milling was analyzed using TEM. In order to breakdown the agglomeration of the powder, ultrasonic was used and several different solvents were tried, including heptane, xylene, and toluene. Xylenes gave the best results. The particle size after 9 hours of milling is in the range of 3 to 20 nm, as shown in the TEM micrographs in Fig. 18.

Due to the uncertainty of the nature of the particles, several other techniques were used to examine the powder, including SEM, XRD, and small angle X-ray scattering(SAXS).

The SEM micrograph of Fig. 19 shows the morphology of the powder milled for 0.5 hour, which has some nano particles agglomerated onto the large particles. The SEM micrograph of Fig. 20 shows the morphology of the powder milled for 9 hours, which has many nano particles agglomerated together or onto some larger particles. By observing the SEM micrographs, some nanoparticles with less than 100 nm in size can be distinguished from the agglomerations.

Table 4 lists the grain sizes of the powders milled in various hours, which were estimated from XRD by using software. Longer milling time resulted in smaller grains size, with 22 nm after 0.5 hour milling down to 10 nm after 9 hours milling. We believe that a longer milling time caused many defects, such as cracks and distortions in the crystal structure and crystal lattice, and the XRD pattern shows smaller grains for the crystalline with these defects. Some research group reported that 0.5 hour milling resulted in 20 nm nanoparticles, and it was likely that the grain size was mistakenly reported as the particle size^[17-18] since it was highly unlike that 0.5 hour milling could result in all the nanoparticles with particle size \leq 20 nm.

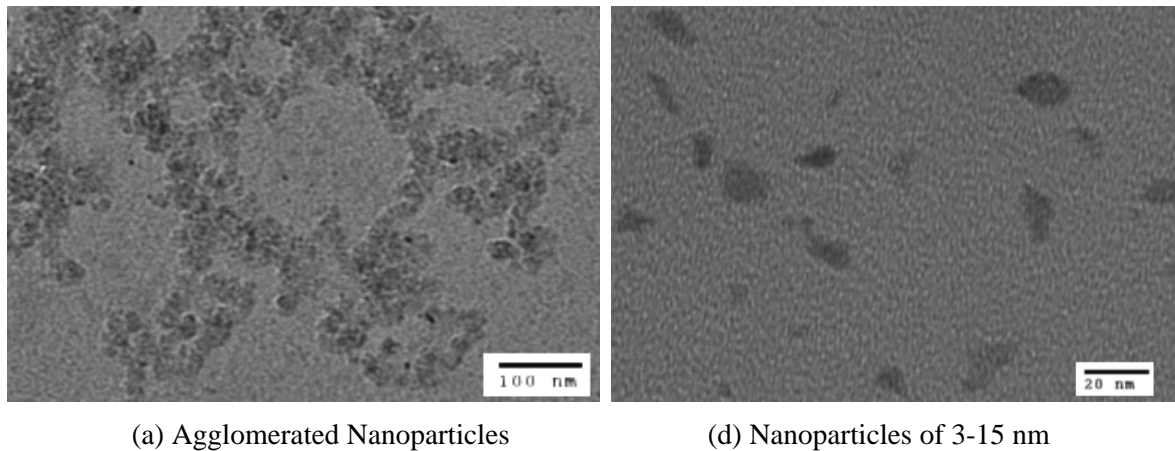


Fig. 18: TEM Micrographs of Nd-Fe-B Nanoparticles

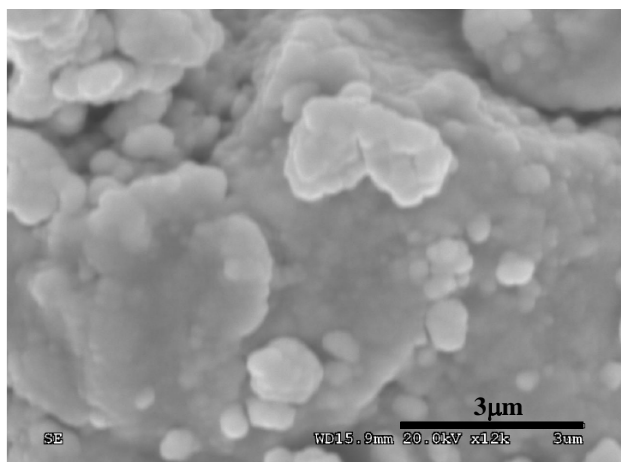


Figure 19: SEM Microstructures of the Powders Milled for 30 Minutes.
Some Nanoparticles are Agglomerated onto the Surface of Large Particles

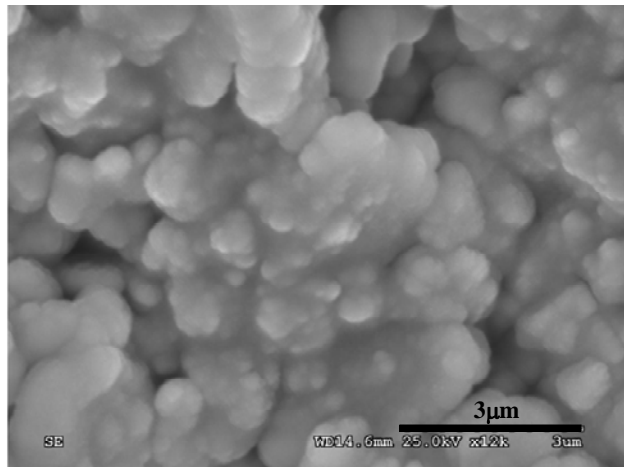


Figure 20: SEM Microstructures of the powders milled for 9 hours.
Many nano particles are agglomerated together or onto some larger particles

Table 4 Grain Size Estimated from XRD Patterns by Software

Note: Grain size \neq Particles size

Sample #	Grain Size from XRD patterns
0.5 H	22 nm
1.5 H	19 nm
3 H	14 nm
6 H	11 nm
9 H	10 nm

The SAXS did not give decisive results which can determine the actual particle sizes for the powders milled with various hours. Some of the XRD and SAXS work described above were done by Prof. Ping Liu's group at Texas University at Arlington, since their group has been working on the topic of Nd-Fe-B nano particles since 2004, so far there is little success making any nano particles with meaningful coercivity ^[16]. Our group and Dr. Liu's group will continue collaboration in this topic.

Amorphous metal does not have any anisotropy and coercivity, and less perfect crystal lattice would have lower coercivity. Unlike the mechanical alloyed powder which going through re-crystallization during hot compaction, the surfactant-assistant high energy milled powder did not go through a re-crystallizing step.

3.4 Nanoparticles and bulk of PrCo₅ and SmCo₅

A technique using high energy ball milling with surfactant assistance was reported to prepare nanoparticles such as SmCo₅, Sm₂Co₁₇, Nd₂Fe₁₄B, and PrCo₅.^[16-18, 20, 22] Up to now, the investigations in this field have focused on the fabrication of nanoparticles, and bulk magnets made from this kind of nanopowders have not been reported. We believe that compacting this type of powder and forming a desired bulk magnet will be the next challenging goal, so we synthesized PrCo₅ nanopowders by surfactant-assisted ball milling and further made an effort to fabricate PrCo₅ bulk magnets by using a RF inductive heating compaction process.

A PrCo₅ alloy was prepared by arc melting in argon using pure metals, with a calculated composition of Pr₁₈Co₈₂ to compensate for Pr loss during processing. The alloy was then crushed and grinded down to less than 250 μ m as the starting powder. The powder was milled in a vial with carbon-steel balls using a Spex 8000M high energy mill. The weight ratio of the balls to the powders is 10:1. Heptane (99.9%) was used as the solvent and oleic acid (90%) was used as the surfactant in the wet milling. The amount of solvent and surfactant used was 55% and 10% of the weight of the starting powders, respectively. After 4 hours of milling, the resultant PrCo₅ slurry was washed by heptane and dried in vacuum. The dried powders loaded into a die were heated to the compaction temperature (200~525°C) in vacuum and meanwhile compacted under a pressure of $\sim 1.7 \times 10^8$ Pa. The obtained PrCo₅ bulk magnets were rod shaped, approximately 8 mm in diameter and ~ 8 -10 mm in length.

Powder samples for magnetic characterization were prepared by mixing the nanoparticles with epoxy inside a glove box and letting it cure in the magnetic field to obtain an aligned sample. A KJS hysteresisgraph and vibrating sample magnetometer (VSM) were used for magnetic measurements. Structural and morphology characterizations were made using XRD, TEM, SEM, and EDS. Powder samples for TEM were prepared by dispersing the as-milled PrCo₅ slurry into heptane with ultrasonic vibrating and drying on carbon coated copper grids.

Figures 21 and 22 show TEM and SEM images of the particles after 4 hours of milling. During the preparation of the powder samples, some powder particles suspended in the solvent after ultrasonic vibration have a particle size of 20 nm or less, as indicated by the TEM image in Figure 1. Meanwhile, the other powders sedimentated gradually, and SEM imaging revealed that these flake-shaped powders' size are usually smaller than 400 nm in thickness and 5 μ m in width as shown in Figure 22. One flake may consist of multi-nanograin chains because of the nanoparticles' agglomeration, and it may be only one big particle. Thus, PrCo₅ powders after 4 hours of milling consist of round-shape nanoparticles and flake-shaped particles. SEM/EDS analysis on the milled powder is shown in Fig. 23 (a). It is obvious that there is no Fe in the milled powder, thus Fe contamination from milling vial and balls didn't happen during the milling process.

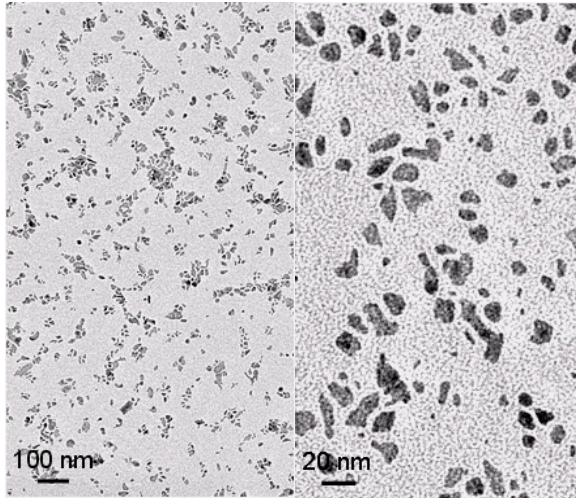


Figure 21: TEM Images of the Particles Suspended in the Solvent

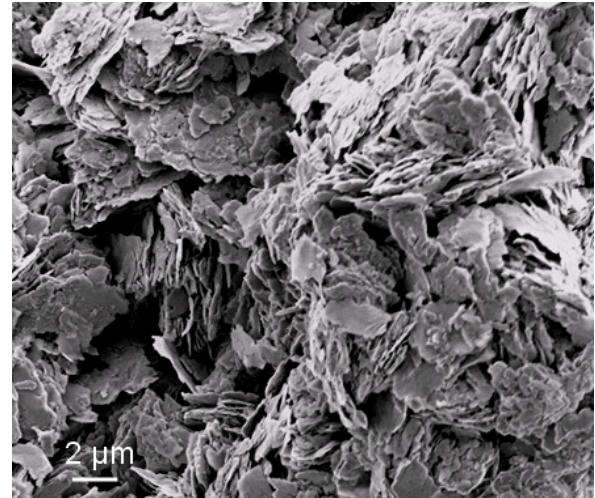


Figure 22: SEM Image of the Particles Sedimentated at the Bottom of the Solvent

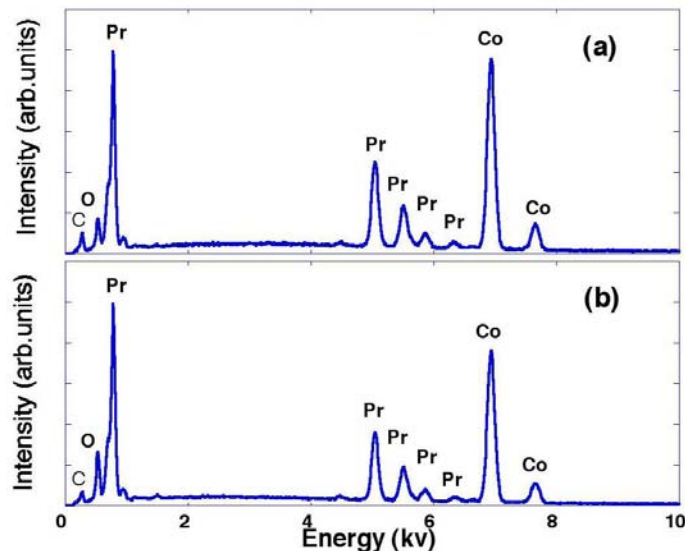


Figure 23: SEM/EDS Results for the PrCo5 Powder and Bulk:
 (a) Powder Milled 4 h; (b) Bulk Pressed at 200°C

The VSM test result of a nanoparticle in epoxy sample is shown in Figure 24. The M-H curves indicate a $B_r(x)/B_r(z)$ ratio of ~ 0.6 and an intrinsic coercivity of 6.67 kOe, demonstrating anisotropic behavior. Here, $B_r(x)$ and $B_r(z)$ present the remanence perpendicular and parallel to the aligned field direction, respectively.

After reducing the surfactant content, the nanopowder was successfully compacted to bulk samples. A bulk sample pressed at 200°C revealed almost the same XRD patterns as the milled powder (Figure 25). The diffraction peaks of the starting powder show a small amount of $\text{Pr}_5\text{Co}_{19}$ phase in addition to the main phase of PrCo_5 . The broadening peaks for both the as-milled

powder and the bulk reveal a fairly small crystallite size. As seen in Figure 26, the SEM image of the bulk shows several flake particles fused together as a “cluster”, which may consist of multi-nanograins. This cluster type structure matches the morphology of the milled powders as described earlier. The evidence above indicates the compaction at 200°C did not change the crystalline structure of the particles. The intrinsic coercivity of the bulk sample pressed at 200°C was slightly reduced to 5.22 kOe as seen in Figure 27. Figure 23 shows the oxygen content in the bulk is slightly higher than that in the powder, which may result in the coercivity of the bulk being lower than that of the powder.

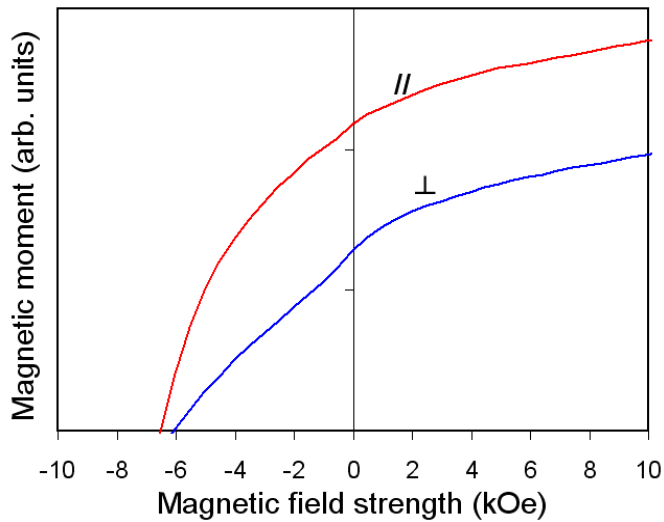


Figure 24: Magnetization Curves of 4 Hour Milled PrCo₅ Powder Epoxy Sample by VSM

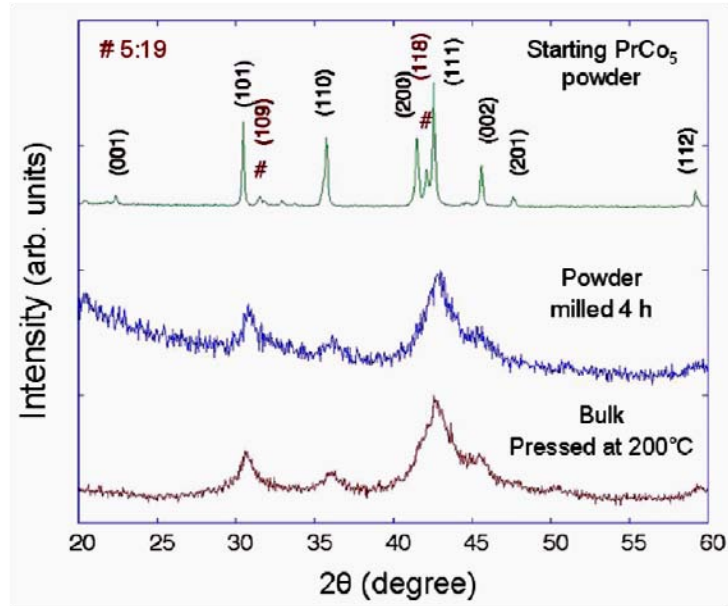


Figure 25: XRD Patterns for PrCo₅ Starting Powder, Milled 4 Hours Powder, and Bulk Pressed at 200°C

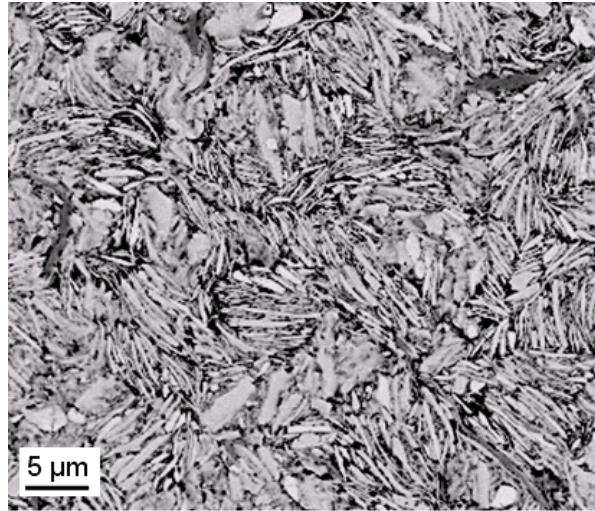


Figure 26: SEM Image of PrCo_5 Bulk Compacted at 200°C

The bulk magnet pressed at 200°C has a density of 6.26 g/cm³. As the pressing temperature increases from 200°C to 300, 400 and 525°C, the bulk becomes denser, as shown in Figure 27. The highest density is 7.70 g/cm³, 92% of theoretical density; however, the coercivity decreases as the temperature increases. XRD analysis for the bulk magnets pressed at 400 and 525°C indicates the existence of PrO_2 peaks and cobalt peaks, resulting in a decrease of coercivity. Since the grain growth is not significant at temperatures below 525°C for this alloy, the decrease in coercivity is likely related to the loss of praseodymium due to oxidization and the appearance of a cobalt phase. In this pressing process, the oxygen likely came from two sources, one from the residual oxygen in the vacuum chamber and another from the residual oleic acid of powders. The as-milled powder was washed three times in heptane, and most of the surfactant oleic acid was likely dissolved into heptane. But it is difficult to totally remove oleic acid absorbed on the particle surface. Further investigation on the effect of surfactant on the compaction process and the bulk properties is under way.

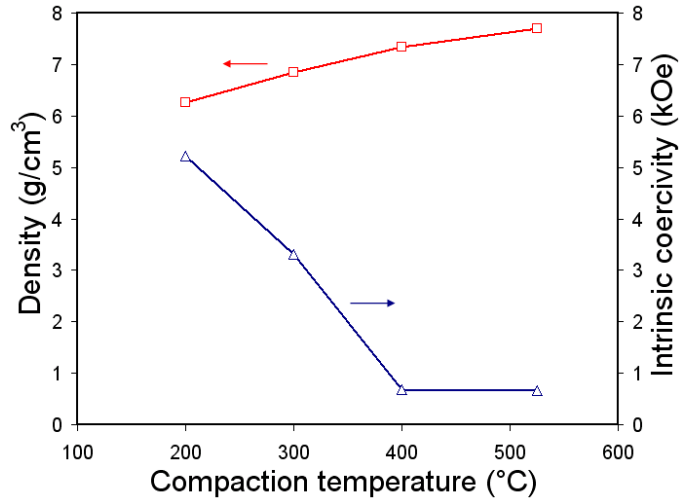


Figure 27: Effect of Pressing Temperature on the Coercivity and Density of PrCo_5 Bulk

3.5 Magnetic Characterization in Closed-Circuit Measurements

3.5.1 The Phenomenon of Magnetization Distortion in the Closed-Circuit Measurements

Magnetic measurements made under “open-circuit” conditions, typically using a VSM with the sample placed in the gap of an electromagnet, are subject to error from what is known as the *image effect*^[24-26]. The flux pattern produced in space around the magnetized sample is distorted by the presence of the large, high-permeability pole pieces of the electromagnet. At high fields, the pole pieces begin to approach magnetic saturation, and the flux lines surrounding the saturated area go through varied paths. This was named the image effect by Weiss^[24-25]. The usual result of the image effect is an apparent drop in the measured magnetization as the pole pieces approach saturation. Correction for the image effect is difficult since the effect depends on the size and shape of the sample, the geometry of the measuring coils and of the electromagnet, and because it varies with the degree of saturation of the electromagnet pole pieces.

Closed-circuit measurements are generally not considered subject to the image effect^[26]. However, when measuring permanent magnet samples clamped between the pole pieces of an electromagnet, we observe a phenomenon similar to the image effect, as shown in Fig. 28^[27]. The drop in apparent magnetization can appear in quite low fields and can be large, approaching 50%. The effect depends on the length-to-diameter ratio of the sample, and becomes minimal for L/D greater than about 1.8. In order to understand this behavior and determine its cause, a series of experiments has been conducted using various sample materials and L/D ratios.

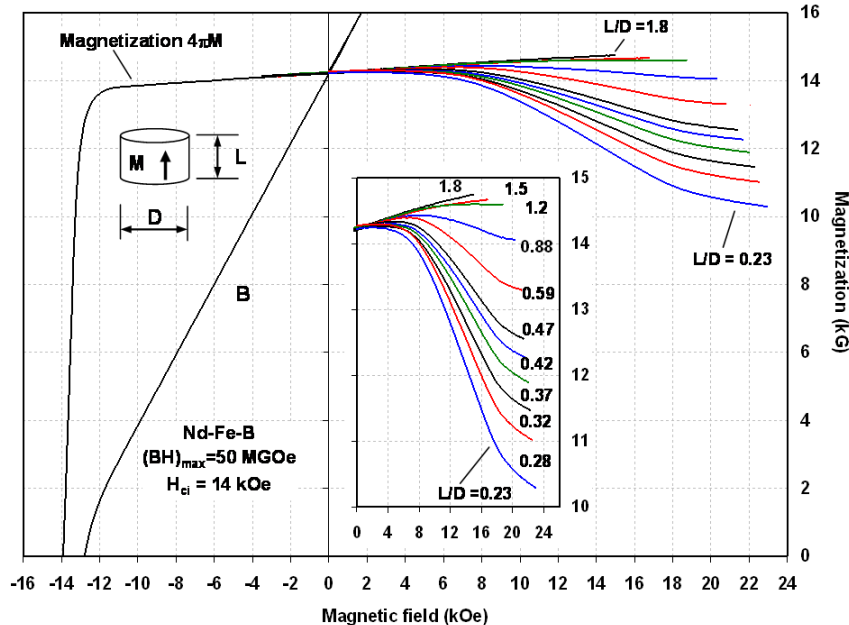


Figure 28: Magnetization Distortion in Closed-Circuit Testing of Nd-Fe-B Magnets with Different L/D Values

Several series of cylindrical specimens 1.2 cm in diameter were made with a range of L/D values from 0.23 to 1.8. The materials used included permanent magnet materials of Nd-Fe-B (50 MGOe) and 2:17 type Sm-Co (28 MGOe), and soft magnetic materials of 1018 steel and nickel. Magnetic induction (flux density) B was measured with a centrally-located coil surrounding the sample, and the field intensity H about 1.5 mm outside the sample was measured with a pair of concentric coils of slightly different diameters connected in series opposition. The voltages from the flux and field coils are separately integrated and continuously recorded to give values of B and H as the electromagnet current is varied. At the start of each measurement and prior to sample insertion, the integrating flux-meters for B and H are adjusted for minimum drift and reset to zero. The sample is then put in the coil set, the sample/coil assembly is placed into the gap of the electromagnet, and the sample is clamped between the electromagnet's movable Fe-Co pole pieces as shown in Fig. 29. Values of B and H are recorded as the current in the electromagnet is varied. The magnetization is given by $B - H = 4\pi M$ (gauss).

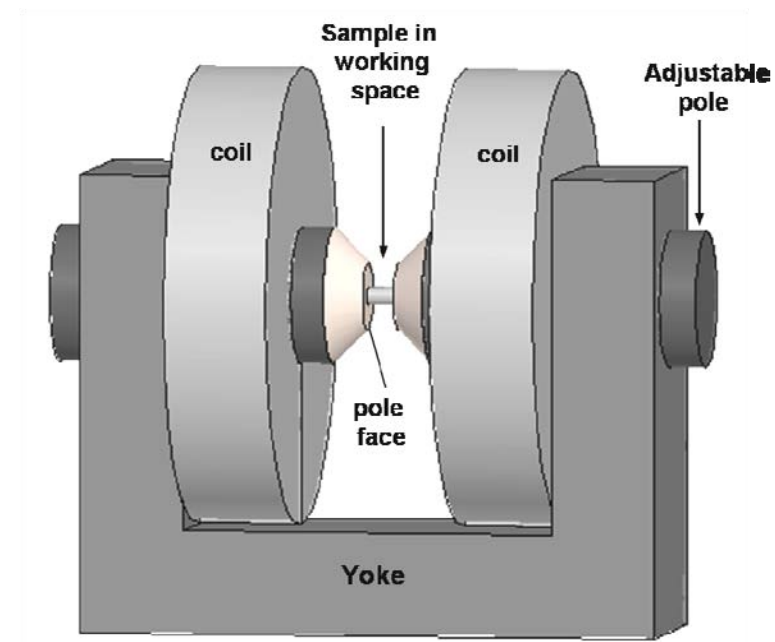
To establish a baseline, magnetic field H and magnetic induction B were measured with no sample present in a series of air gaps from 0.29 to 2.55 cm. In all measurements the electromagnet was driven with a maximum ampere-turns. In all cases, the measured values of B were linear with the measured values of H , and $B - H$ was zero for all values of H . A hysteresigraph (KJSA/Magnetic Instrumentation, Inc. Model HG-700) was used for the closed-circuit magnetic measurements.

The measured results for Nd-Fe-B with ten different values of L/D ranging from 0.23 to 1.8 are shown in Fig. 28. The measured results for 1018 Steel with five different L/D values ranging from 0.23 to 1.8 are shown in Fig. 30. The measurement results for 1018 steel, Nd-Fe-B, and nickel, each with $L/D = 0.30$ and $L = 0.377$ cm, as well as a measurement with no sample present (labeled "air"), are shown in Figures 31 to 33. Figure 31 shows lines of both B and $4\pi M$ on the same graph; Fig. 32 shows $4\pi M$ and Fig. 33 shows B , both for only positive values of H .

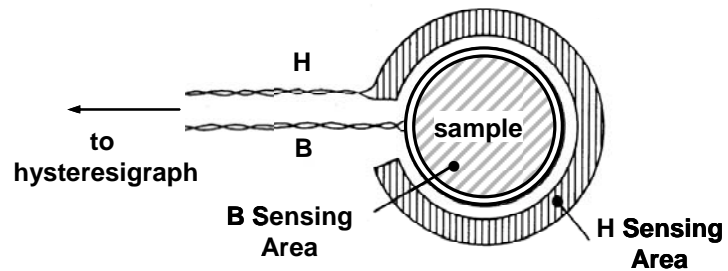
With no sample present, (labeled "air"), B is linear with H and $4\pi M$ is zero, showing that the coils are properly calibrated. When a magnetic specimen is present between the pole-tips of the electromagnet, the apparent value of $4\pi M$ decreases with increasing applied field. The apparent decrease in magnetization is greater, and the field at which it appears is lower, as the saturation magnetization of the sample material increases.

Note that the measured maximum field also decreases as the saturation magnetization of the sample increases, even though the electromagnet was driven to the same maximum value of ampere-turns in each case. This means that the measured value of H as well as the measured value of B is reduced by the presence of the magnetic sample.

The values of the apparent decreases in $4\pi M$ and in H were determined as shown in Fig. 32, and the apparent drop in B as in Fig. 33. The numerical values of the decreases are collected in Tables 5 and 6. The decreases in $4\pi M$ and in H are plotted vs. the measured maximum magnetization of the samples in Fig. 34. The straight line corresponds to a constant 23% difference.



(a) Sample/Pole-Piece Configuration (Sample Length can Vary)



(b) Schematic Drawing of Pick-up Coils (Not to Scale)

Figure 29: Setup of Closed-Circuit Magnetic Measurement for Closed-Circuit Measurements

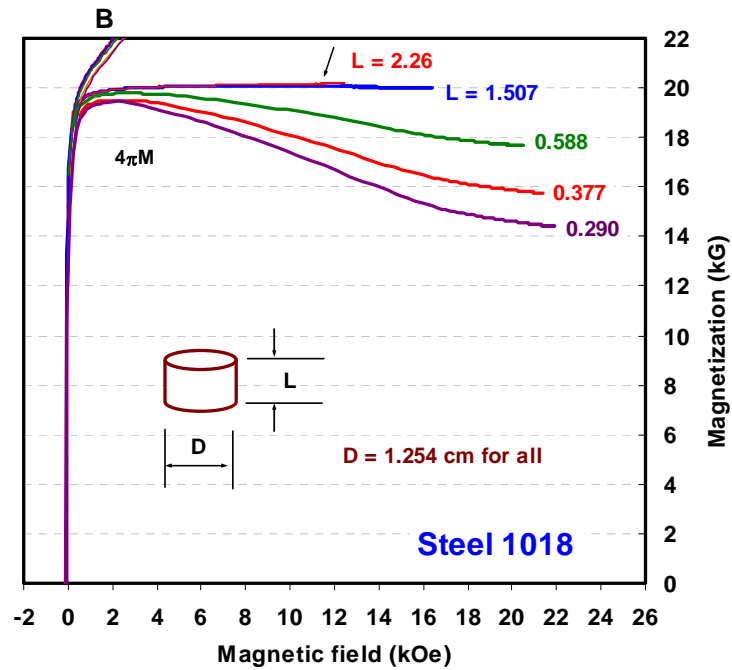


Figure 30: Magnetization Distortion in Closed-Circuit Testing of 1018 Steel with Different L/D

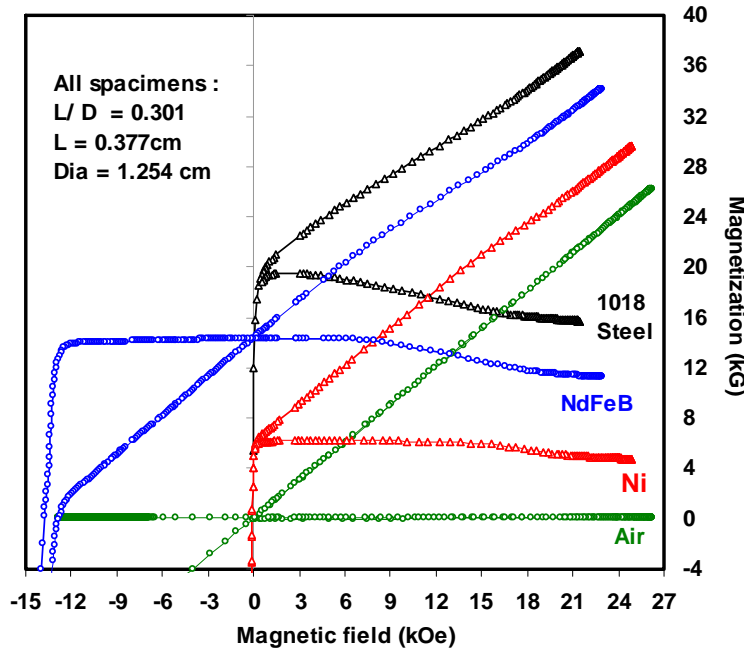
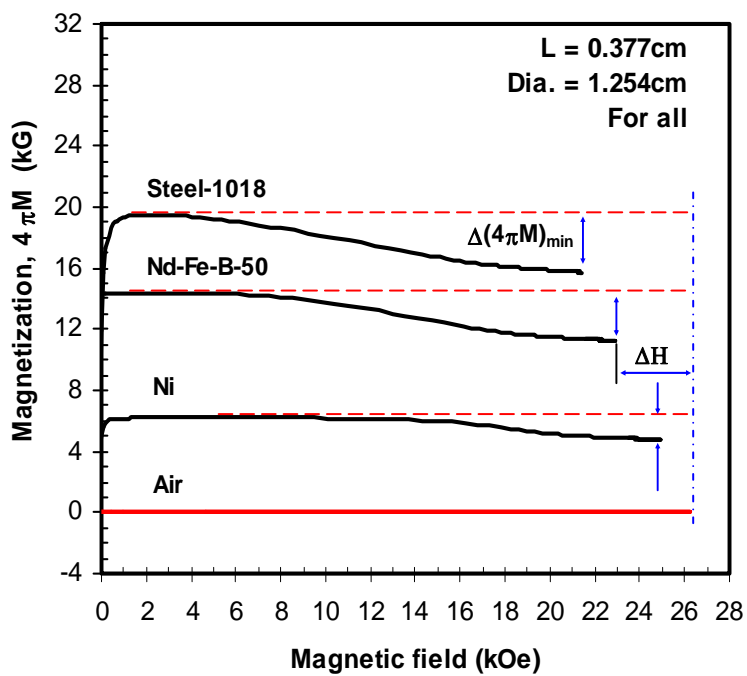
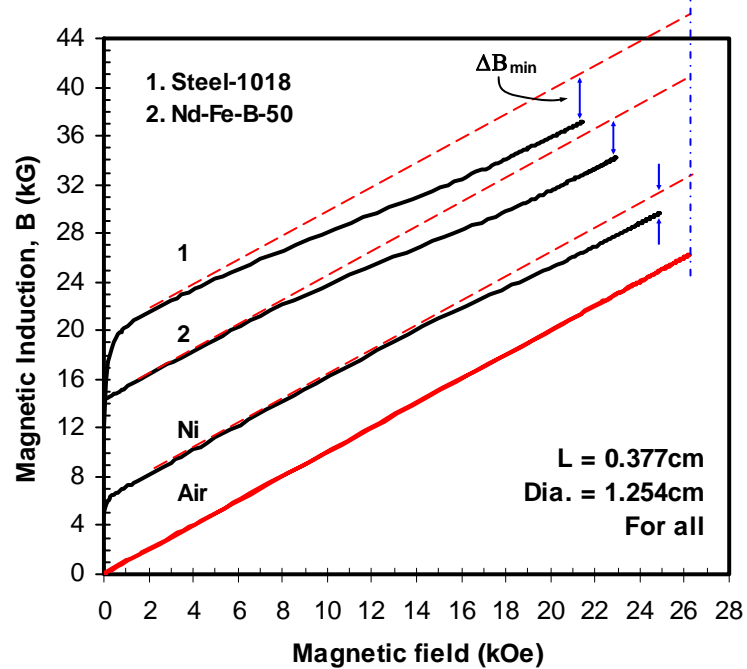


Figure 31: Magnetization Curves for Four Materials with $L/D = 0.30$ ($L = 0.377 \text{ cm}$) Tested in Closed-Circuit



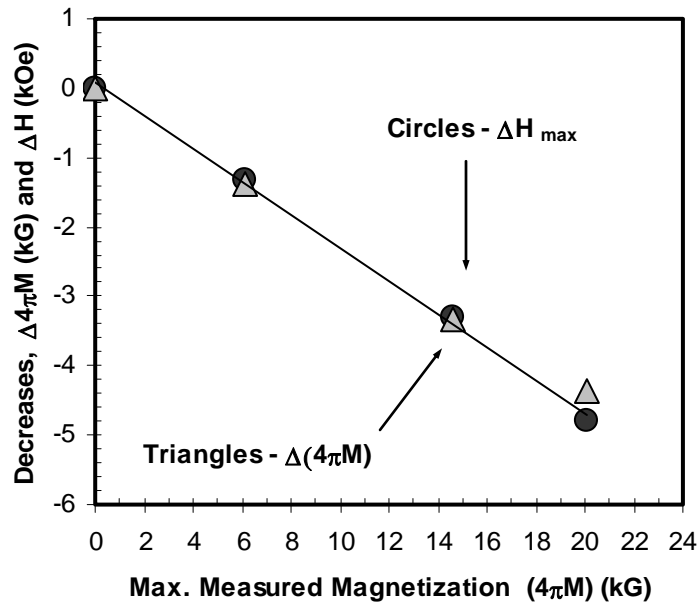


Figure 34: Decreased Values of $4\pi M$ and H vs. Maximum Magnetization of Measured Materials

Table 5. Magnetic Fields and Inductions Obtained in Closed-Circuit Measurement at 4300 Ampere-Turns

Specimen Material	Magnetic field (kOe)		Magnetic induction (kG)		
	H_{max}	ΔH_{max}	B	B_{tan}	ΔB
1018 steel*	21.4	-4.8	37.2	41.1	-3.9
Nd-Fe-B*	22.9	-3.3	34.2	37.5	-3.3
Ni *	24.9	-1.3	29.7	31.5	-1.8
Air *	26.2	0	26.2	26.2	0

* Lengths and air gaps are the same for these specimens (0.377 cm).

Table 6. Magnetization Obtained in Closed-Circuit Measurement at 4300 Ampere-Turns

Specimen Material	Magnetization (kG) at the H_{max} listed in Table 5		
	$4\pi M$	$4\pi M_{max}$ *	$\Delta 4\pi M$
1018 steel	15.74	20.1	-4.36
Nd-Fe-B	11.26	14.6	-3.34
Ni	4.78	6.15	-1.37
Air	0	0	0

* The $4\pi M_{max}$ is the maximum magnetization in the curve of $4\pi M$ vs. H , as shown in Fig. 33.

3.5.2 Analysis of the Distortion Using Computer Modeling

Our attributed the distortion in closed-circuit measurement described the last section to the distortion of the magnetic flux distribution around the sample, resulting from local saturation of the electromagnet pole pieces. Computer modeling was employed to confirm the explanation.

Computer modeling was carried out using Ansoft Maxwell 3D v.12 software. The computer model was set up to correspond to our experimental arrangement as shown in Fig. 29. The samples were cylinders of 1018 steel with $D = 12.56$ mm and $L = 2.9, 5.3, 11.1$, and 22.6 mm, resulting in L/D ratios of 0.23, 0.42, 0.88 and 1.8, respectively. The samples were clamped between the Fe-Co pole pieces of an electromagnet. Steel was chosen as the sample material because it has a higher saturation magnetization than any permanent magnet material, and shows the apparent image effect more strongly and at lower applied field. Therefore, steel samples represent a worst-case situation. The electromagnet was driven with a large number of ampere-turns, corresponding to its maximum safe operating power. At the resulting field levels the steel samples were completely saturated. All the calculations were made with at least six adaptive passes of mesh refinement with each pass having 10 to 20 nonlinear iterations. Iterations were repeated until values for energy error and delta energy were less than 0.10%.

Figure 35 shows the magnetic field distribution in and around the samples when maximum power was applied to the electromagnet, for long ($L/D=1.8$) and short ($L/D=0.23$) samples. Figure 36 is a plot of calculated H vs. position along a diameter at the mid-plane of the sample and electromagnet air gap for four different values of L/D , and Fig. 37 shows the same data normalized so that 100% represents the value of the field in the air gap when no sample is present. The sample diameter and the position of the co-axial H pickup coils are indicated by dashed lines. A schematic drawing of the pickup coils can be seen in Fig. 29b.

The amplitude of the maximum applied field increases as the sample length decreases, because the electromagnet air gap becomes smaller with the same ampere-turns of excitation. For $L/D=1.8$, the field at the sample center and surface is uniform. For smaller L/D the field becomes increasingly non-uniform. For the shortest sample ($L/D=0.23$), the field varies from 14.5 kOe at the sample center to 24 kOe at the sample surface, and continues to increase to 29 kOe at ~ 12 mm outside the sample.

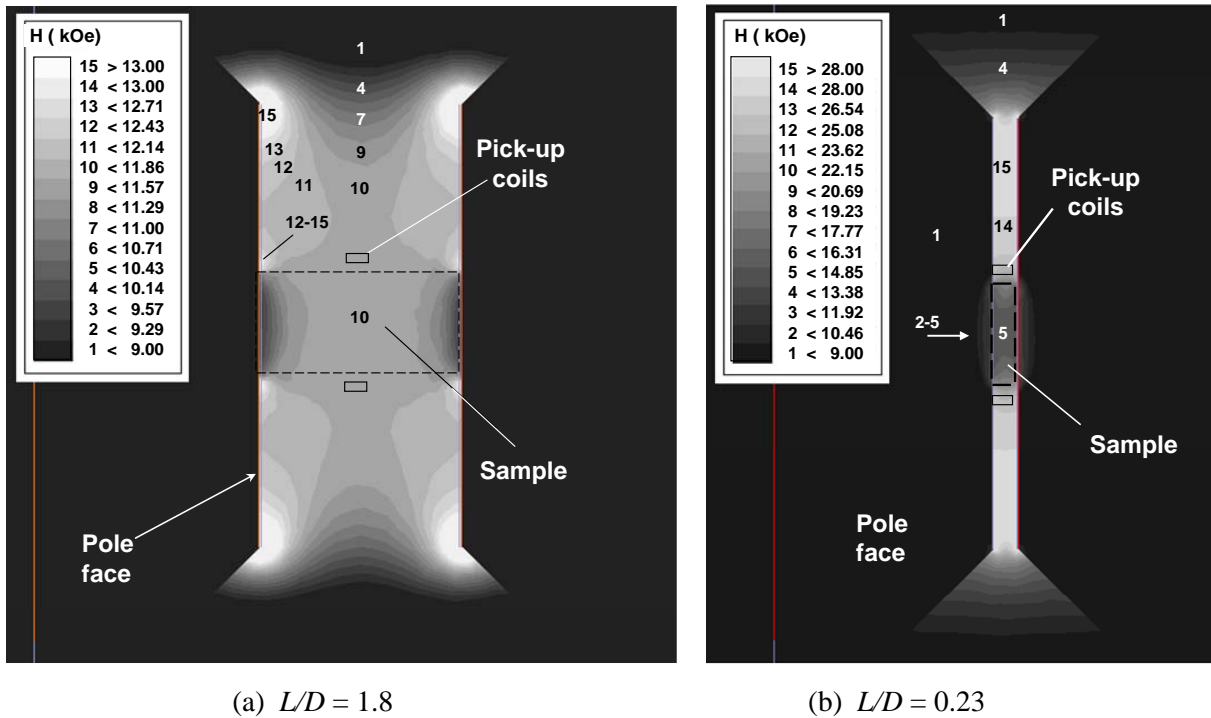


Figure 35: Calculated Field Distribution in Closed-Circuit Testing of 1018 Steel Samples

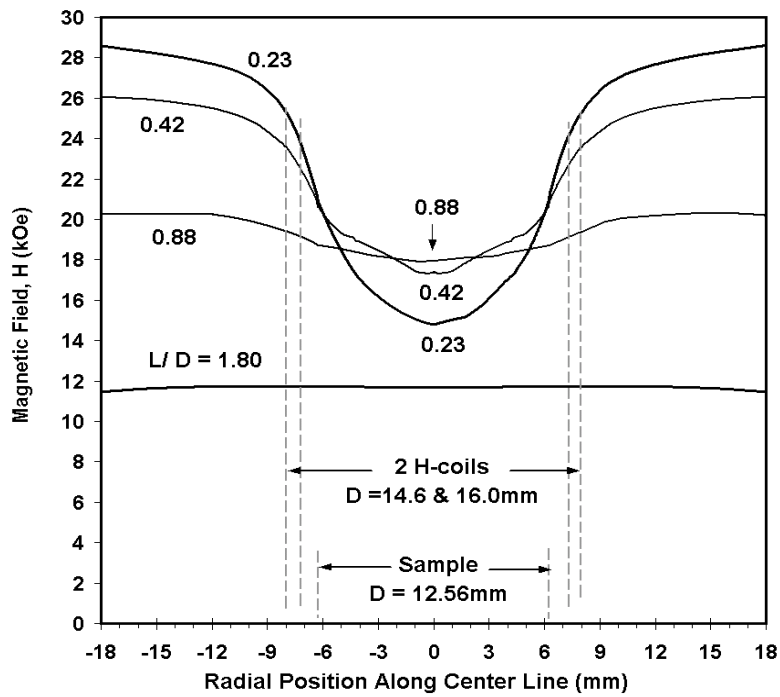


Figure 36: Calculated Magnetic Field Values vs. Radial Position Along the Midplane Through the Samples with Varying L/D

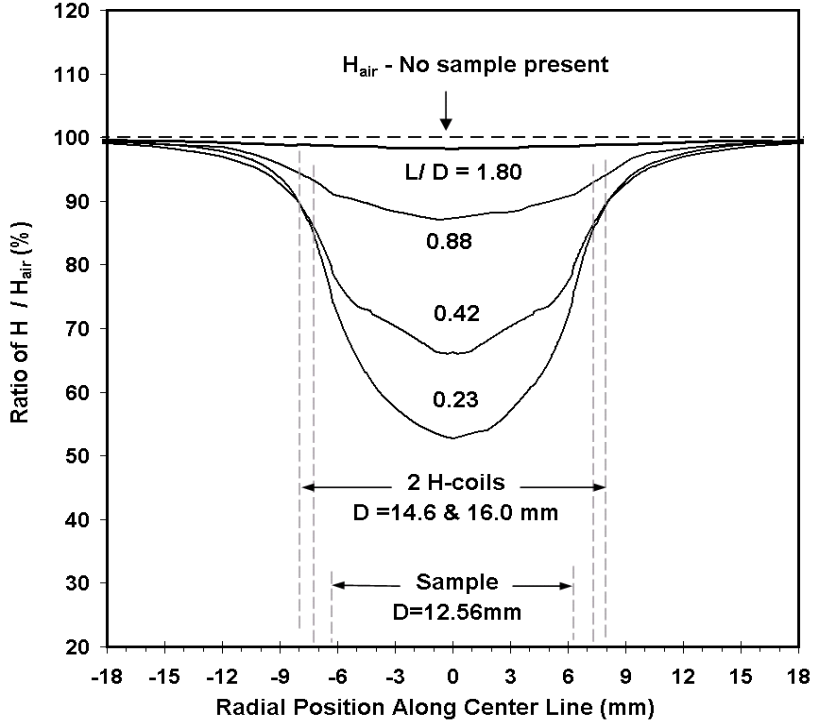


Figure 37. Normalized Calculated Magnetic Field Values vs. Radial Position Along the Midplane Through the Samples with Varying L/D

Figure 38 shows the flux density B in and around samples with $L/D=1.8$ and 0.23 under the same conditions as for Fig. 35. Saturation of the samples and of the region in the pole pieces immediately adjacent to the ends of the samples is clearly seen, as is the non-uniform field distribution in the electromagnet air gap near the ends of the samples.

Figures 39 and 40 plot the calculated field along horizontal lines parallel to the electromagnet and sample axis, where R denotes the radial distance in mm from the center line. Figure 39 is for $L/D=0.23$; Fig. 8 for $L/D=1.8$. Values of $R < 6.28$ are inside the sample and values of $R > 6.28$ are outside the sample. The inner and outer H pickup coils are at $R=7.3$ and $R=8$, respectively, with axial length 2 mm. Figure 39 clearly shows that the field outside the sample is substantially higher than the field inside the sample at all points along the sample length. By contrast, in Fig. 40 the field is quite uniform over the central 8 mm of the sample, and reasonably uniform ($\pm 10\%$) over the entire sample length. Figures 41 and 42 plot values of B rather than H . Values are not shown for $R > 6$, since outside the sample $B=H$.

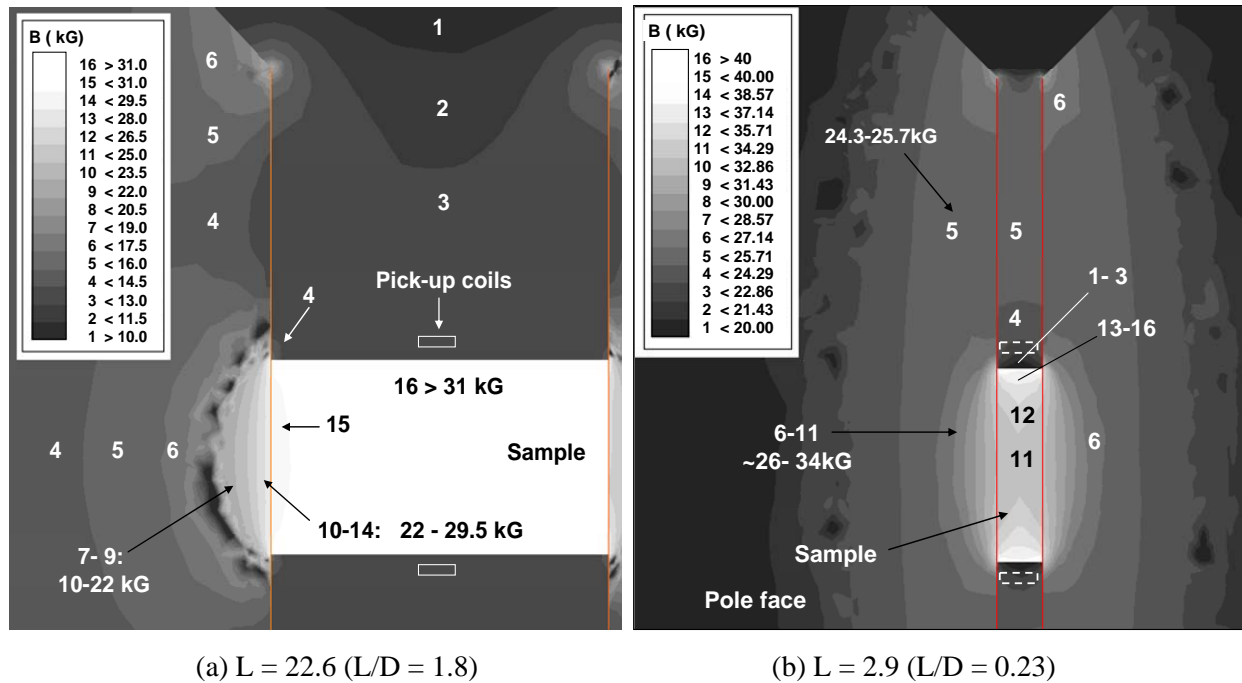


Figure 38: Calculated Distribution of Flux Density B in
Closed-Circuit Testing of 1018 Steel Samples

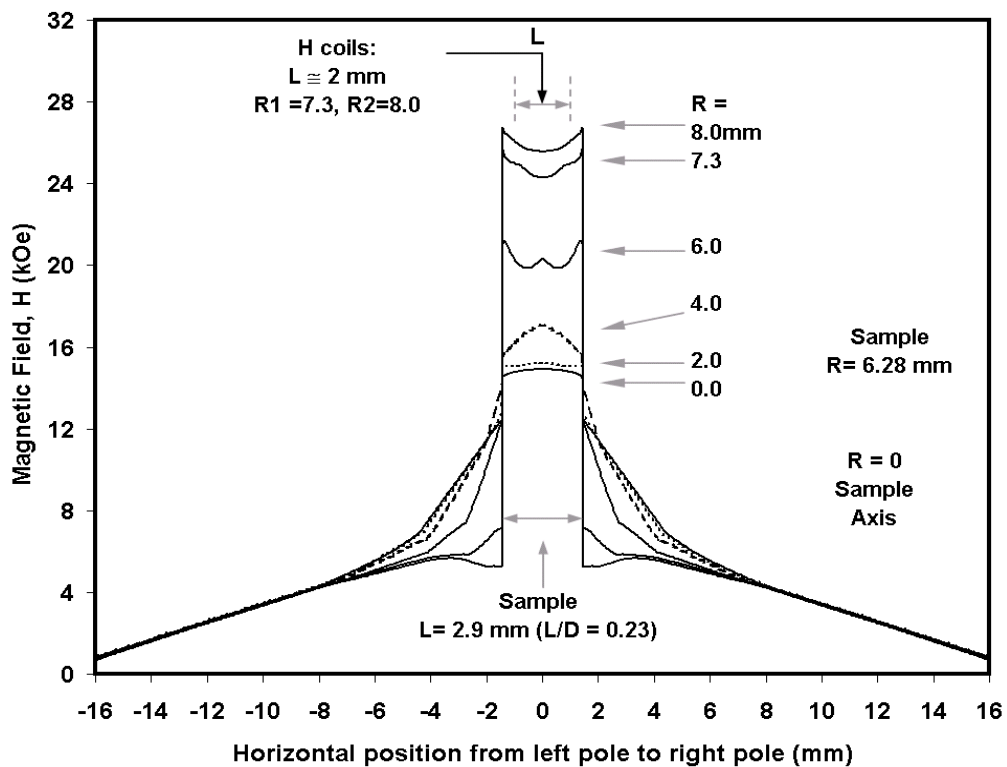


Figure 39: Calculated Field H Along Lines Parallel to the Magnet / Sample Axis for
the Sample with $L/D = 0.23$

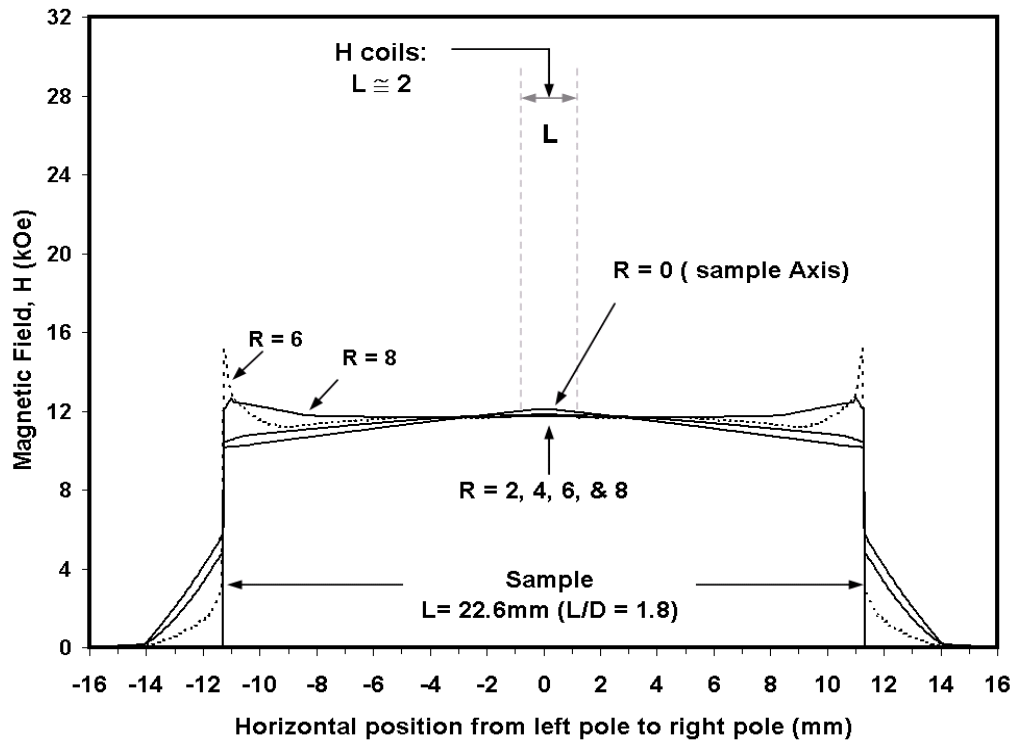


Figure 40: As Figure 37, for Sample with $L/D = 1.8$

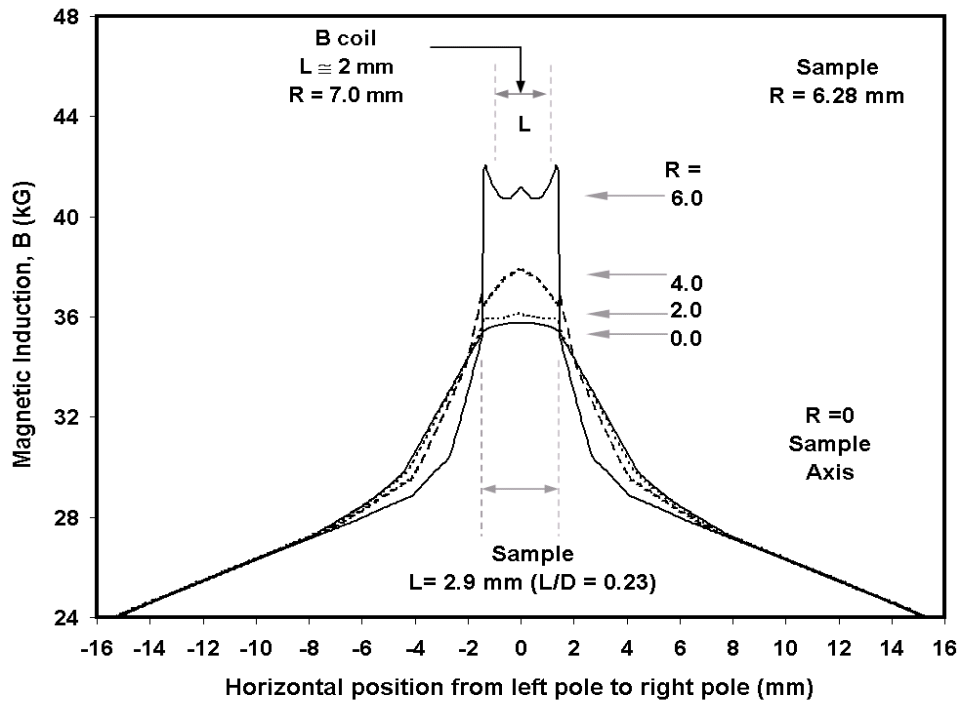


Figure 41: Calculated Flux Density B Along Lines Parallel to the Sample /Magnet Axis for the Sample with $L/D=0.23$

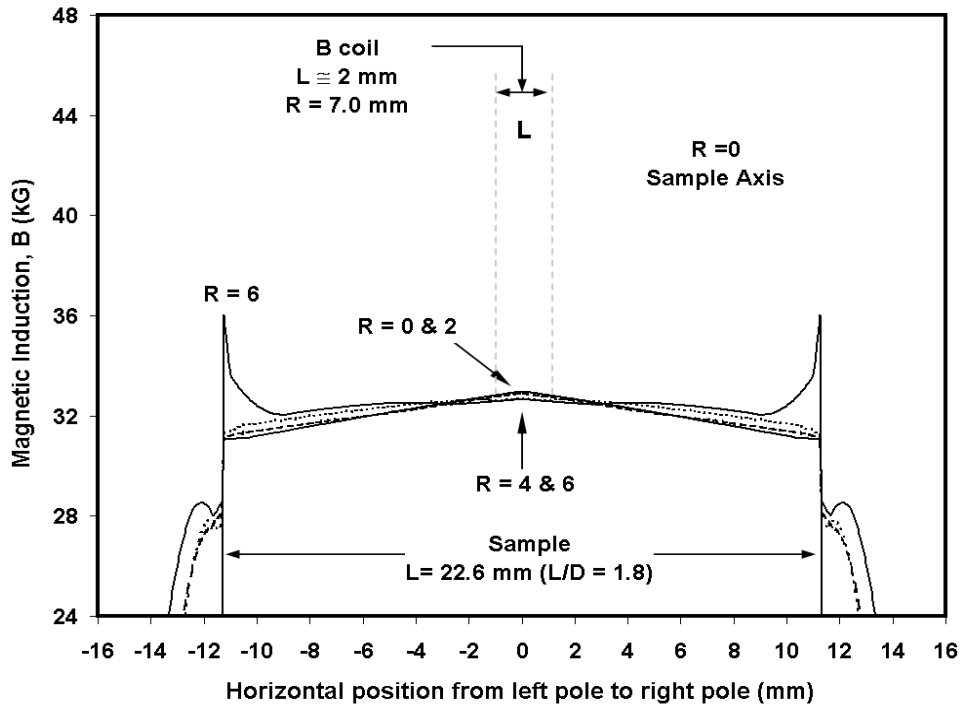


Figure 42: As Figure 41, for Sample with $L/D=1.8$

For short samples, the value of field measured at the position of the pickup coils is clearly much higher than the field acting at any point inside the sample. Since the value of magnetization ($4\pi M$) is obtained by subtracting the measured H from the measured B ($4\pi M = B - H$), an erroneously high value for H leads to an erroneously low value for $4\pi M$. The calculated results are consistent with measured data. Thus the apparent image effect in closed-circuit measurements is due to a non-uniform field created by local saturation of the electromagnet pole pieces.

4.0 CONCLUSIONS AND RECOMMENDATIONS

4.1 Nanocomposite of Rare Earth Hard Phases and Fe-Co soft Phase

Using current techniques, including powder coating, HP and HD, nanostructured magnets with ~ 1-3% soft-phase were made with an improvement in energy products (~5 to 8%) compared to the magnets without a soft-phase, but the process could not result in $(BH)_{max} > 56$ MGOe. A larger volume of soft-phase and a special microstructure are required for higher energy product, which have an optimum separation between the soft phase and the hard-phase of nanograins for an effective exchange coupling. Such required microstructure can only be produced using innovative techniques which have yet to be established.

In addition to the required microstructure, the grain-growth effect and the interdiffusion between the hard and the soft phases must be eliminated. Further more, the hard and the soft phases in a bulk magnet must be uniformly dispersed on the nano-scale while minimizing the oxygen content. Three major challenges must be overcome before achieving significant progress:

- 1) A novel process will be needed to disperse the nanograins of the hard and soft phases with oxidation content < 0.10 wt%;
- 2) A unique process will be necessary to make fully dense bulk magnets with process temperatures < 300°C to avoid the detrimental interdiffusion;
- 3). New techniques will be required to make anisotropic powders with nanograins and achieve better than 95% alignment of the magnets with nanograins at process temperatures < 300°C.

Recommendations for further research efforts are as follows:

- 1) “Bottom-up” routine starting with nanoparticles should be used. Nanoparticles should be made under protection media, and novel technique should be developed.
- 2) Modified surfactant-assistant high energy milling may be one of the novel processes for synthesizing nanoparticles, which may also make nano-scale dispersed two distinct phases simultaneously.
- 3) Modified magnetic dynamic compaction (MDC) should be employed to consolidate the powder into full density at temperature less than 300°C. Aligning field should be applied simultaneously during compaction.

4.2 Nanoparticles of Rare Earth Permanent Magnetic Phases

PrCo_5 nanopowder can be produced by surfactant-assisted high energy ball milling. The powders consist of round-shape nanoparticles and flake-shaped particles. The intrinsic coercivity of the powders milled 4 hours is 6.7 kOe. Using the nanopowders, PrCo_5 bulk magnets have been successfully fabricated by compaction at 200~525°C. The bulk magnet has a cluster microstructure with nanocrystallinity. It is found that the density of the bulk increases with the

compaction temperature. Bulk magnet density up to 92% of the theoretical value has been obtained. The coercivity of the bulk magnet decreases as the compaction temperature increases because of oxidation during processing. Modified MDC should be employed to consolidate the powder into full density at temperature less than 300°C. Aligning field should be applied simultaneously during compaction. Aligning field should be applied simultaneously during compaction, which should be developed in further research work.

The material of Nd-Fe-B phase is much tougher than RE-Co phase. Due to the mechanical stress and strain, high energy milling very likely result in large particles or amorphous nanoparticles. The crystallized spin-cast ribbon powder was used as the starting powder, which has isotropic nanograins, and it is impossible to make anisotropic powder using current technology. If the cast-alloy anisotropic powder with large grains would be used, the difficulty of making nanoparticles would be increased due to non-grain-boundary breaking.

One possibility is to use the deformed Nd-Fe-B bulks as the starting powder which has nanograins with large aspect ratio in ab-plane and c-axis of the crystalline, like the anisotropic grains obtained after hot deformation. The breaking places can along the grain boundaries during the high energy milling, and the nanoparticles would have less stress and strains, which can retain the anisotropic properties and coercivity.

4.3 Magnetic Characterization in Closed-Circuit Measurements

We have come to the following conclusions:

- The apparent image effect occurs for both hard and soft magnetic materials, with H_{ci} from about 10 Oe to more than 20,000 Oe and $4\pi M_s$ from about 6 to more than 20 kG.
- Both the B and the H signals are affected and reduced.
- The drop in apparent magnetization occurs at lower fields for materials with higher magnetic saturation.
- The presence of a sample lowers the measured maximum field H at a given gap, and the decrease is larger for sample material with higher saturation magnetization.
- The magnitude of the effect decreases as the sample length and distance between the pole-pieces increases, and becomes negligible as the distance approaches 2.5 cm.
- The effect appears only in the first and third quadrants of the hysteresis loop.

Computer modeling confirms that the apparent image effect in close-circuit magnet testing can be explained by distortion of the field around the sample caused by local saturation of the pole tips just under the ends of the sample. Modeling also shows that in samples with low values of the ratio of length to diameter (L/D), the field in the sample is seriously non-uniform, so that even an accurate measurement of the field at the sample surface would not give a valid point on the magnetization curve.

Further analyses are required in order to establish a method for making correction for the error occurs in the 1st and 3rd quadrants.

5.0 REFERENCES

- [1] Matsuura, Y., “Recent development of Nd–Fe–B sintered magnets and their applications,” *J. Magn. Magn. Mater.* 303, 2006, p. 344.
- [2] Buschow, K.H.J., “Permanent magnet materials based on 3d-rich ternary compounds,” *Ferromagnetic Materials* 4, 20, Elsevier Science Publishers B.V. (1988).
- [3] Strnat, K.J., “Rare earth-cobalt permanent magnets,” *Ferromagnetic Materials* 4, 154, Elsevier Science Publishers B.V. (1988).
- [4] Ray, A.E. and Strnat, K.J., “Research and development of rare earth-transition metal alloy as permanent magnet materials,” Technical Report AFML-TR-73-276, 1973, p. 26.
- [5] Kneller, E.F. and Hawig, R., “The exchange-spring magnet: a new material principle for permanent magnets,” *IEEE Trans. Magn.* 27, 1991, p. 3588.
- [6] Skomski, R. and Coey, J.M.D., “Giant energy product in nanostructured two-phase magnets,” *Phys. Rev. B* 48, 1993, p. 15812.
- [7] Chen, C.H., Walmer, M.S., Walmer, M.H., Liu, S. and Kuhl, G.E., “Thermal stability at 300-550°C for a new series of $\text{Sm}_2\text{TM}_{17}$ materials with maximum use temperature up to 550°C,” *IEEE Trans. Magn.* 36 (5), 2000, p. 3291.
- [8] Lee, D., Hilton, J.S., Liu, S., Zhang, Y., Hadjipanayis, G.C., and Chen, C.H., “Hot Pressed and Hot Deformed Nanocomposite $(\text{Nd},\text{Pr},\text{Dy})_2\text{Fe}_{14}\text{B}$ / α -Fe Based Magnets,” *IEEE Trans. Magn.* 39 (5), 2003, p. 2947.
- [9] Lee, D., Hilton, J.S., Chen, C.H., Huang, M.Q., Zhang, Y., Hadjipanayis, G.C., and Liu, S., “Bulk Isotropic and Anisotropic Nanocomposite Rare Earth Magnets,” *IEEE Trans. on Magn.* 40 (5), 2004, p. 2904.
- [10] Liu, S., Higgins, A., Shin, E., Bauser, S., Chen, C., Lee, D., Shen, Y., He, Y. and Huang, M.Q., “Enhancing Magnetic Properties of Bulk Nanograin Composite Nd-Fe-B/Fe-Co Magnets by Applying Powder Coating Technologies,” *IEEE Trans. Magn.* 42 (10), 2006, p. 2912.
- [11] Wecker, J., Katter, M., and Schultz, L., “Mechanically alloyed Sm-Co materials,” *J. Appl. Phys.* 69, 1991, p. 6058.
- [12] Ding, J., McCormick, P.G., and Street, R., “Metastable Phase Formation in Mechanically Alloyed Sm-Co-Fe,” *J. Alloys Comp.* 191, 1993, p. 197.
- [13] Ding, J., McCormick, P.G., and Street, R., “A study of $\text{Sm}_{13}(\text{Co}_{1-x}\text{Fe}_x)_{87}$ prepared by mechanical alloying,” *J. Magn. Magn. Mater.* 135, 1994, p. 200.
- [14] McCormick, P.G., Miao, W.F., Smith, P.A.I., Ding, J., and Street, R., “Mechanically alloyed nanocomposite magnets,” *J. Applied Physics* 84 (11), 1998, pp. 6256-6261.
- [15] Wang, Y., Li, Y., Rong, C., and Liu, J.P., “Sm-Co hard magnetic nanoparticles prepared by surfactant-assisted ball milling,” *Nanotechnology*, 18, 2007, p. 465701.

- [16] Yue, M., Wang, Y.P., Poudyal, N., Rong, C.B., and Liu, J.P., “Preparation of Nd–Fe–B nanoparticles by surfactant-assisted ball milling technique,” *J. Appl. Phys.* 105, 2009, p. 07A708.
- [17] Akdogan, N.G., Hadjipanayis, G.C., and Sellmyer, D.J., *J. Appl. Phys.* 105, 2009, p. 07A710.
- [18] Akdogan, N.G., Hadjipanayis, G.C., and Sellmyer, D.J., EG-07 presented at *INTERMAG 2009*, California.
- [19] Zeng, H., Li, J., Wang, Z.L., Liu, J.P., and Sun, S., “Bimagnetic Core/Shell FePt/Fe₃O₄ Nanoparticles,” *NanLetters* 4, 2004, pp. 187-190.
- [20] Chakka, V.M., Altuncevahir, B., Jin, Z.Q., Li, Y., and Liu, J.P., “Magnetic Nanoparticles Produced by Surfactant-Assisted Ball Milling,” *J. Appl. Phys.* 99, 2006, p. 08E912.
- [21] Elkins, K.E., Chaubey, G.S., Nandwana, V., Liu, and J. Ping, “A Novel Approach to Synthesis of FePt Magnetic Nanoparticles” *J. Nano Research* 1, 2008, pp. 23-29.
- [22] Wang, Y., Li, Y., Rong, C., and Liu, J. Ping, “Sm-Co hard magnetic nanoparticles prepared by surfactant-assisted ball milling,” *Nanotechnology* 18, 2007, p. 465701.
- [23] Weiss, P. and Forrer, R., “Magnetization and magnetocaloric phenomena of nickel,” *Ann de Physique* (10) 5, 1926, p. 171.
- [24] Weiss, P. and Forrer, R., “The absolute saturation of ferro-magnetic and laws of approach according to the field and the temperature,” *Ann de Physique* (10) 12, 1929, p. 279.
- [25] Allen, R.I. and Constant, F.W., “The absolute saturation of cubic cobalt,” *Physical Review*, 44, 1933, p. 228.
- [26] Cullity, B.D., and Graham, C.D., Introduction to Magnetic Materials, second ed., IEEE-Wiley, ISBN 978-0-471-47741-9, 2009, p. 70.
- [27] Chen, C.H., Higgins, A.K., and Strnat, R.M., “Effect of geometry on magnetization distortion in closed-circuit magnetic measurements,” *J. Magn. Magn. Mater.* 320 (9), 2008, pp. L84-L87.

APPENDIX – PUBLICATIONS RESULTED FROM THIS PROGRAM

A. Published Papers

1. Chen, C.H., Higgins, A.K., Huang, M.Q., Horwath, J.C., Shen, Y., and Liu, S., “Bulk nanocrystalline $\text{Sm}(\text{Co}_{1-x}\text{Fe}_x)_z$ with 35% Co-Fe phase and the effect of fluorine inclusion,” *J. Appl. Phys.* 105, 2009, p. 07A718.
2. Chen, C.H., Shen, Y., Huang, M.Q., Higgins, A.K., Detrio, J.A., and Liu, S., “Process temperature dependence of the coercivity of nanostructured Nd-Fe-B / Fe-Co composites,” *Proc. of 20th Int'l. Workshop on Rare earth Permanent Magnets and Their Applications*, Crete, Greece, September 2008, pp. 344-347.
3. Higgins, A.K., Graham, C.D., Strnat, R.M., and Chen, C.H., “Apparent image effect in closed-circuit magnetic measurement,” *IEEE Trans. Magn.* 44(11), 2008, pp. 3269-3271.
4. Chen, C.H., Higgins, A.K., and Strnat, R.W., “Effect of Geometry on Magnetization Distortion in Closed-Circuit Magnetic Measurements Journal of Magnetism and Magnetic Materials,” *J. Magn. Magn. Mater.* 320 (9), 2008, pp. L84-L87.
5. Chen, C.H., Huang, M.Q., Bovda, O.M., Bovda, V.O., Chebotarev, V.V., Fedorchenko, V.D., Medvedev, S.V., Onischenko, L.V., Tortika, A.S., Lee, D., Higgins, A., and Liu, S., “Microstructure and Magnetic Property of Nanocomposite of Nd-Fe-B and α -Fe made with PVD coating and Hot Deformation,” *Proc. ISC FMMN 2008*, 2008, pp. 139-141.

B. Submitted two papers under reviewing:

1. Shen, Y., Huang, M.Q., Higgins, A.K., Liu, S., Horwath³, J.C., and Chen, C.H., “Preparation of PrCo_5 bulk magnets using nanopowders made by surfactant-assisted high energy milling,” submitted to *J. Appl. Phys.*, 2009.
2. Chen, C.H., Graham, C.D., Strnat, R.M., Pugh, B.K., Wangler, A., and Higgins, A.K., “Analysis of the Apparent Image Effect in Closed-Circuit Magnetic Measurements by Computer Modeling,” submitted to *IEEE Trans. on Magnetics* (2009).

C. Coauthored published papers:

1. Huang, M.Q., Turgut, Z., Chen, Z.M., Shen, Y.H., Lee, D., Higgins, A., Chen, C.H., Liu, S., Liu, J.F., Horwath, J.C., and Fingers, R.T., “Coercivity of bulk anisotropic nanocomposite $\text{Sm}(\text{CoFeTi})_{8-10}$ magnets,” *J. Appl. Phys.* 105, 2009, p. 123915.
2. Bovda, O.M., Bovda, V.O., Chen, C.H., Garkusha, I.E., Leonov, S.O., Onischenko, L.V., Tereshin, V.I., and Tortika, O.S., “PVD Ti coatings on Sm-Co magnets,” VANT Vacuum, Pure Materials (Ukraine), *Superconductors* 1, 2008, pp. 189-192.
3. Fedorchenko, V.D., Bovda, A.M., Bovda, V.A., Chen, C.H., Chebotarev, V.V., Garkusha, I.E., Liu, S., Medvedev, A.V., and Tereshin, V.I., “ECR plasma-assisted PVD deposition of α -Fe thin film on melt-spun Nd-Fe-B alloys,” *AIP Conf. Proc.* 993, 2008, pp. 403-406.

4. Bovda, O.M., Bovda, V.A., Chebotarev, V.V., Chen, C.H., Fedorchenko, V.D., Higgins, A.K., Medvedev, O.V., Onischenko, L.V., and Tortika, O.S., "Magnetic and microstructure study of anisotropic Nd₂Fe₁₄B/α-Fe nanocomposite magnet by applying PVD coating technology," *Proceedings of 20th International Workshop on Rare Earth Permanent Magnets and Applications* (Crete, Greece), 2008, pp. 210-213.
5. Yue, M., Niu, P., Li, Y., Zhang, D., Liu, W., Chen, C.H., Liu, S., Lee, D., and Higgins, A., "Structure and magnetics of bulk isotropic and anisotropic Nd₂Fe₁₄B/a-Fe permanent magnets with different a-Fe content," *J. Appl. Phys.* 103, 2008, p. 07E101.
6. Huang, M., Ma, B., Lee, D., Chu, S., Turgut, Z., Chen, Z., Higgins, A., Chen, C.H., Liu, S., Horwath, J.C., and Fingers, R.T., "Effects of Zr, Nb and Cu substitutions on magnetic properties of melt-spun and hot deformed bulk anisotropic nanocomposite SmCo type magnets," *J. Appl. Phys.* 103, 2008, p. 07E134.
7. Sirisha, K., Chen, Q., Ma, B.M., Huang, M.-Q., Chen, C.H., and McHenry, M.E., "Effect of Ga substitution on the structure and magnetic properties of melt-spun Pr₃(Fe,Co,Ti)₂₉ system," *J. Appl. Phys.* 101, 2007, p. 09K512.